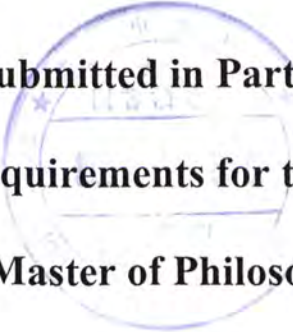


# **Height Inspection of Wafer Bumps without Explicit 3D Reconstruction**

by

**DONG, Mei**

**A Thesis Submitted in Partial Fulfillment  
of the Requirements for the Degree of  
Master of Philosophy**



**In**

**Automation and Computer-aided Engineering**

**©The Chinese University of Hong Kong**

**March 2007**

The Chinese University of Hong Kong holds the copyright of this thesis. Any person(s) intending to use a part or whole of the materials in the thesis in a proposed publication must seek copyright release from the Dean of the Graduate School.



**Thesis/ Assessment Committee**

Professor HUI Kin-Chuen (Chair)  
Professor CHUNG Chi-Kit, Ronald (Thesis Supervisor)  
Professor WANG Yu, Michael (Committee Member)  
Professor YUNG H. C. Nelson (External Examiner)

# ABSTRACT

The shrunk dimension of electronic devices leads to more stringent requirement on process control and quality assurance of their fabrication. For instance, direct die-to-die bonding requires placement of solder bumps not on PCB but on the wafer itself. Such wafer solder bumps, which are much miniaturized from their counterparts on PCB, still need to have their heights meet the specification, or else the electrical connection could be compromised, or the dies be crushed, or even the manufacturing equipments be damaged. Yet the tiny size, typically tens of microns in diameter, and the texturelessness and mirror nature of the bumps pose great challenge to the 3D inspection process.

This thesis addresses how a large number of such wafer bumps could have their heights massively checked against the specification. The idea is based on the thought of problem conversion, that is, from the problem of height inspection to the problem of top points investigation, then to the problem of two planes investigation. It involves an extraction and reforming of the top points on the bumps, and in this way to avoid the explicit 3D reconstruction. The measure possesses these advantages: (1) it is sensitive to global and local disturbances to the bump heights, thus serving the bump height inspection purpose; (2) it is invariant to how individual bumps are locally displaced against one another on the substrate surface, thus enduring 2D displacement error in soldering the bumps onto the wafer substrate; and (3) it is largely invariant to how the wafer itself is globally positioned relative to the imaging system, thus having tolerance to repeatability error in wafer placement.

This measure makes use of the mirror nature of the bumps, which used to cause difficulty in traditional inspection methods, to capture images of two planes. One contains the top points of the bumps and the other corresponds to the substrate. With the homography matrices of these two planes and fundamental

matrix of the imaging system, we synthesize a matrix about the disparity of the two planes. This matrix can summarize the bumps' heights in a fast and direct way without going through explicit 3D reconstruction. We also present a design of the imaging and illumination setup that allows the measure to be revealed in two images, and how the inspection measure could be estimated from the image data so acquired. Both synthetic and real data experimental results are shown to illustrate the effectiveness of the proposed system.

## 摘 要

電子器材日益精細的尺寸結構，引發對其製造流程中過程控制和質量保證的更高要求。例如，芯片與芯片之間的直接鍵合需要將焊點置於晶片自身而非電路印刷板上。這些焊點的尺寸比電路印刷板上的焊點小很多，而且對高度有非常嚴格的要求，否則將會直接影響成品電路連接，甚至導致芯片和製造設備的損壞。而它們直徑約為幾十至幾百微米的尺寸，和光滑呈鏡面反射性且不具紋理的焊點表面，都給相關的三維檢測帶來很大的困難。

本文著眼於對多個球形焊點高度的平行測量，針對焊點陣列，提出了一種新穎的檢測方法。本算法基於問題轉化的思想，即將高度檢測的問題轉化為對於焊點頂點的考察，進而轉化為對於兩個特殊平面的考察，其過程涉及到對與焊點頂點的提取和重組，從而避免了額外的三維重建。本算法具有以下優點：（1）對於整個焊點陣列或陣列中個別焊點的高度變化非常敏感，因此可直接用於焊點高度測量；（2）與陣列中焊點的二維排列無關，因此對於焊點的平面分佈具有較強的容錯性；（3）對於芯片的整體位移具有較強的容錯性。

本算法利用了傳統算法中被視為障礙的焊點鏡面反射特性，以此獲得兩個平面的影像。一個平面包含了大部分的球形焊點頂點，另一個平面與芯片底板相對應。利用兩個平面的單應性矩陣和攝像系統的基本矩陣，合成了一個雙平面差矩陣。對於該矩陣的分析可直接獲得焊點陣列的高度信息。我們將同時闡述專為此算法設計的影像系統，以及具體的操作方法和計算過程。合成數據實驗及真實芯片處理結果都證明了該算法的有效性。



## ACKNOWLEDGEMENT

I would like to express my most sincere thanks to my supervisor, Prof. Ronald CHUNG Chi kit, for all his help during the past years. His guidance and encouragement were vital elements in the completion of this work.

I would also like to thank ASM automation assembly Ltd. for their project and their great help in the experiments and their support for my research. I would like to say thank you to Prof. Edmund Lam, Dr. Kenneth Fung, Dr. WANG fan for their kind help and advices in every student meeting.

I would like to remember all the colleagues and friends who shared with me a lot of happiness during my study. To name only some of them: Mr. Cheng Jun, Mr. Chim Ho-Ming, Mr. He Yong, Mr. Liang Bodong, Mr. Song Zhan, Mr. Wang Wei, Ms. Yuan Ding.

Finally I wish to express my deepest gratitude to my family for their always supporting and for their continuous encouragement.

(The work was substantially supported by a grant from the Innovation and Technology Commission of Hong Kong Special Administrative Region, China, under an Innovation and Technology Fund with Project Code UIM/111.)

Dong Mei

# CONTENTS

<b>INTRODUCTION.....</b>	<b>1</b>
1.1 Bump Height Inspection .....	1
1.2 Our Height Inspection System .....	2
1.3 Thesis Outline .....	3
 <b>BACKGROUND .....</b>	 <b>5</b>
2.1 Wafer Bumps .....	5
2.2 Common Defects of Wafer Bumps.....	7
2.3 Traditional Methods for Bump Inspection.....	11
 <b>BIPLANAR DISPARITY METHOD.....</b>	 <b>22</b>
3.1 Problem Nature .....	22
3.2 System Overview .....	25
3.3 Biplanar Disparity Matrix D .....	30
3.4 Planar Homography .....	36
3.4.1 Planar Homography .....	36
3.4.2 Homography Estimation .....	39
3.5 Harris Corner Detector.....	45
3.6 Experiments .....	47
3.6.1 Synthetic Experiments .....	47
3.6.2 Real image experiment.....	52
3.7 Conclusion and problems.....	61
 <b>PARAPLANAR DISPARITY METHOD.....</b>	 <b>62</b>
4.1 The Parallel Constraint.....	63
4.2 Homography estimation.....	66
4.3. Experiment:.....	69
4.3.1 Synthetic Experiment:.....	69
4.3.2 Real Image Experiment:.....	74
 <b>CONCLUSION AND FUTURE WORK .....</b>	 <b>80</b>
5.1 Summary of the contributions.....	80
5.2 Future Work .....	81



Publication related to this work: ..... 83

BIBLIOGRAPHY ..... 83

List of Figures

Figure 2.1: Solder bumping process flow..... 6

Figure 2.2: The Ball Grid Array (BGA) ..... 7

Figure 2.3a: Bump malformation ..... 9

Figure 2.3b: Bump bridging..... 9

Figure 2.3c: Bump misplacement ..... 9

Figure 2.4: The coplanarity requirement of the wafer bumps ..... 10

Figure 2.5: Principle of Laser scan system ..... 13

Figure 2.6: Principle of confocal system ..... 14

Figure 2.7: Configuration of Moire Interferometry ..... 17

Figure 2.8: 3D Z-topography of bare die showing a bump defect ..... 18

Figure 3.1: Image of the bump grid array ..... 23

Figure 3.2: Image of the substrate ..... 23

Figure 3.3: The two planes reveal the bump height information ..... 26

Figure 3.4: Imaging setting of the Biplanar Disparity Method (BDM) ..... 27

Figure 3.5: The top points will cast the brightest points in the image ..... 28

Figure 3.6: The idea to get the height information by plane parameters ... 30

Figure 3.7: Homography between a 3D plane and its image ..... 37

Figure 3.8: Homography between the two images of a 3D plane ..... 38

Figure 3.9: Norm of BDM in the absence of any error or uncertainty. .... 48

Figure 3.10: Performance of BDM with resolution error ..... 50

Figure 3.11: Performance of BDM with resolution error and global  
transformation error.....50

Figure 3.12: Performance of BDM with resolution error, global transformation error, brightest points determination error...	51
Figure 3.13: The imaging system.....	53
Figure 3.14: The 5 DoF platform for the wafer.....	53
Figure 3.15: The parallel light source for the side camera.....	54
Figure 3.16: A pair of pictures of wafer A in subgroup 1. ....	56
Figure 3.17: A pair of pictures of wafer A in subgroup 2. ....	57
Figure 3.18: A pair of pictures of wafer A in subgroup 3. ....	57
Figure 3.19: A pair of pictures of wafer B in subgroup 1.....	58
Figure 3.20: A pair of pictures of wafer B in subgroup 2.....	58
Figure 3.21: A pair of pictures of wafer B in subgroup 3.....	59
Figure 3.22: Norm of D induced by two different wafers with variant disturbance added.....	60
Figure 4.1a: Some of the bumps are too tall or too short .....	63
Figure 4.1b: The bumps are globally too short (or too tall).....	63
Figure 4.2a: The ideal projection of a certain point on the center image...	71
Figure 4.2b: The projection image of a certain point by BDM.....	71
Figure 4.2c: The projection image of a certain point by PDM .....	72
Figure 4.3a: The noise free output of norm of D by fixed height bumps.....	73
Figure 4.3b: The output of BDM under Gaussian noise. ....	73
Figure 4.3c: The output of PDM under Gaussian noise .....	74
Figure 4.4: Real image for BDM and PDM – Picture pair 1 .....	75
Figure 4.5: Real image for BDM and PDM – Picture pair 2 .....	75

Figure 4.6: Real image for BDM and PDM – Picture pair 3 .....	76
Figure 4.7: Real image for BDM and PDM – Picture pair 4 .....	76
Figure 4.8: Real image for BDM and PDM – Picture pair 5 .....	77
Figure 4.9: Real image for BDM and PDM – Picture pair 6 .....	77
Figure 4.10: Real image for BDM and PDM – Picture pair 7 .....	78
Figure 4.11: Comparison of the performance of BDM and PDM .....	79

List of Tables

Table 3.1: The parameters in synthetic experiments..... 48

Table 3.2: Norm of BDM by wafer A.....59

Table 3.3: Norm of BDM by wafer B ..... 59

Table 4.1: The parameters in synthetic experiments..... 70

Table 4.2: Comparison of the results of BDM and PDM ..... 78

# **Chapter 1**

## **INTRODUCTION**

### **1.1 Bump Height Inspection**

The relentless miniaturization drive together with the demand for high performance and functionality of portable electronics, such as notebook PCs, hand phones and camcorders, translate into the use of smaller electronic packages with high I/O counts operating at high frequencies. Flip-chip [1] is currently the most promising approach to satisfy the high-end packaging requirements. Forecasts [2, 3] show that this advanced packaging technology will find increasing applications in the high-performance products and it could capture as much as one third of the packaging market in the next few years.

Alongside the development of the WLP technology is a demand for improved process control as well as quality assurance. However, because of the much reduced size of the circuitry in wafers or dies in comparison with that of PCBs, the wafer bumps are of much smaller size, typically with a diameter of only tens of microns. Objects of such size are difficult to have their 3D shape reconstructed with enough accuracy, yet even tiny errors on their heights and so on will be a hazard to the bonding process. Because of the mini size of the bumps, visual inspection technologies widely used for PCB bumps are not



applicable. 3D inspection of wafer bumps is a bottleneck to the WLP technology.

One particular and important inspection needed in WLP is to check whether all the bumps on a wafer are of the same and specified height, so as to prevent too loose or too strong contact of a few bumps in the bonding process, in the sense that too loose contact may cause bad connection of components thus result in poor performance of the equipment, while too strong contact may cause short cut of the circuit or even damage of the chip. There have been a few methods developed for it, but they all require explicit 3D reconstruction which is an expensive process especially for dimensions of such a miniature scale.

## **1.2 Our Height Inspection System**

By contrast, we propose a novel inspection measure about the collection of bump heights that possesses these advantages: (1) it is sensitive to global and local disturbances to the bump heights, thus serving the bump height inspection purpose; (2) it is invariant to how individual bumps are locally displaced against one another on the substrate surface, thus enduring 2D displacement error in soldering the bumps onto the wafer substrate; and (3) it is largely invariant to how the wafer itself is globally positioned relative to the imaging system, thus having tolerance to repeatability error in wafer placement.

This measure makes use of the mirror nature of the bumps, which used to cause difficulty in traditional inspection methods, to capture images of two planes. One contains the bump peaks and the other corresponds to the substrate. With the homography matrices of these two planes and fundamental matrix of the camera, we synthesize a matrix called Biplanar Disparity Matrix. This matrix can summarize the bumps' heights in a fast and direct way without going through explicit 3D reconstruction.

We also present a design of the imaging and illumination setup that allows the measure to be revealed in two images. The system consists of two sets of CCD, lens and light sources. Once the system is set up and calibrated, no moving part is involved in the imaging system during the whole inspection process. This will greatly save the time and reduce the external uncertainty. Getting rid of the high requirement of the positioning accuracy in moving parts will also significantly reduce the potential cost. Both synthetic and real data experimental results are shown to illustrate the effectiveness of the proposed system.

### **1.3 Thesis Outline**

In what follows, chapter 2 will give some background knowledge on the bump height inspection and a review of traditional method. This will provide some concept and points serve as the prerequisite for the following parts, such as the bump nature, the inspection requirement, and the technical background of our method.

Chapter 3 and chapter 4 will be the core parts of this thesis, which illustrate our method in detail. Chapter 3 goes into particulars of the Biplanar Disparity Method (BDM), including the methodology, the relevant computer vision technique, the system setting and operating. Both synthetic and real data experiment results are given. Chapter 4 goes to a further step, introducing the Parallel Disparity Method (PDM), the improved version of the BDM.

Finally the conclusions are made and some future work is suggested in the author's point of view.

## **Chapter 2**

### **BACKGROUND**

#### **2.1 Wafer Bumps**

Flip-chip solder-bump interconnection, the face-down soldering of integrated circuit (IC) devices to chip carriers, has been in manufacturing for nearly forty years [4]. First introduced in 1964 with the solid logic technology in the IBM System/360\*, it was designed to extend interconnection capabilities beyond the existing wire-bonding techniques [5]. Unlike wire bonding, the area array solder-bump configuration allows the entire surface of the chip (die) to be populated with solder bumps that are subsequently interconnected to a substrate by the C4 (controlled collapse chip connection) solder reflow process for the highest possible I/O counts in order to meet the ever-increasing demand for electrical functionality and reliability in IC technology. Although wire bond still dominates IC interconnects in terms of absolute numbers, flip-chip packaging is poised for continued strong growth as it gains in many applications previously dominated by wire-bond technology, due primarily to the improvements afforded by C4 in such aspects as electrical performance, functionality, and reliability.

Fig. 2.1 simply describes the process flow of the solder bumping. After the process the bumps are typically arranged in a grid array fashion called Ball Grid

Array (BGA) as Fig. 2.2 and serve several functions in the flip chip assembly. Electrically, the bump provides the conductive path from chip to substrate. The bump also provides a thermally conductive path to carry heat from the chip to the substrate. In addition, the bump provides part of the mechanical mounting of the die to the substrate. Finally, the bump provides a spacer, preventing electrical contact between the chip and substrate conductors, and acting as a short lead to relieve mechanical strain between board and substrate.

Wafer bumping process allows die interconnects and chip scale packaging to be manufactured at wafer level, providing high performance devices and cost savings to both manufacturers and end-users. However, the wafer bumping process requires high speed and precise measurement of the height and coplanarity of all of the solder or gold bumps that is vital to ensure electrical connection between the die and a package or circuit board.

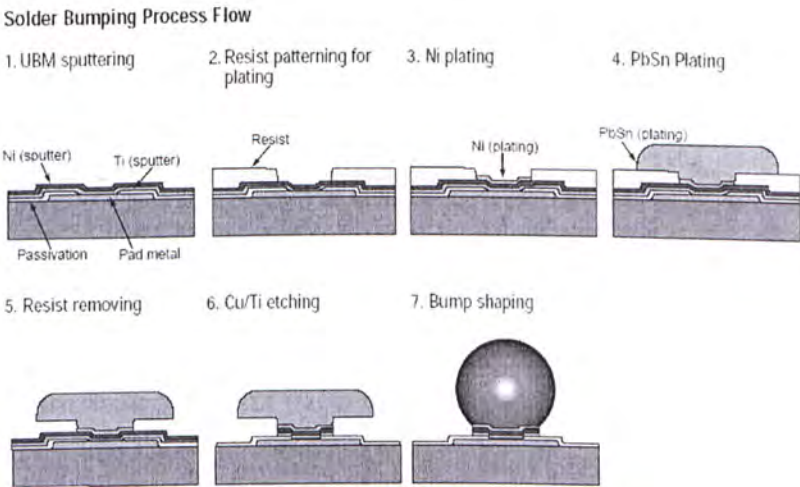


**Figure 2.1: Solder bumping process flow**



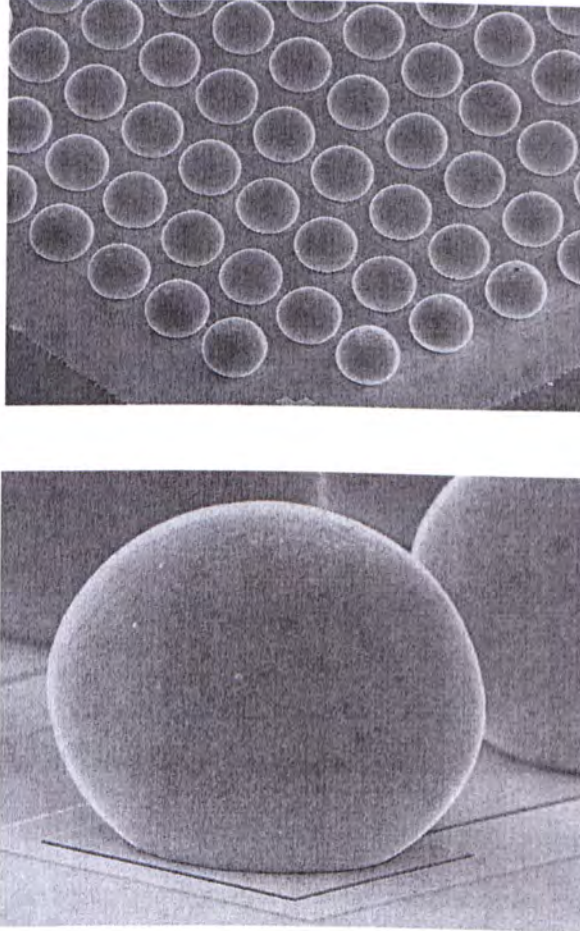


**Figure 2.2: The Ball Grid Array (BGA)**

## **2.2 Common Defects of Wafer Bumps**

All measurement values have user selectable limits. Any value out of the preset limit will be flagged as defect. Typically, 2D inspection is needed for detection,



review and classification of defects. There are also sustained advancements in the manufacturing process that demands better vision inspection algorithms to maintain high through-put and accuracy. For wafer-level packaging, 3D metrology and inspection is also required. Critical measurements are height, diameter (for special bumps), length and width (for rectangular bumps), coplanarity and true position. Of all of these measurements, by far height and coplanarity are two key features. Bumped die whose I/O contact points fail to conform to strict height and coplanarity dimensional tolerance represent a potential electrical failure downstream. A profound bump height or coplanarity problem can cause a probe needle to break during the probing process resulting in a massive financial loss.

## **2D defects**

Some defects, such as missing bumps or bridges between bumps, which are shown below, immediately affect the functionality of the final package. Other defects, such as bump malformation, bump misplacement and inter-bump surface contamination and change in diameter of bumps will affect the product's long-term reliability. Typically, a CCD camera is used to collect images for these measurements and defect identification. The combination of dark field and bright field lighting is used to provide the correct illumination to highlight the area or the feature of interest. Inspection methodologies covering 2D features are fairly standard whether they are for metrology or surface defects.

Sometimes, people use image processing to extract the features, and with some signal processing traditional method to deal with the images, thus find these defects.

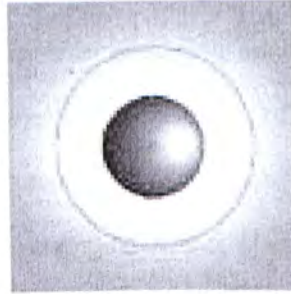


**Figure 2.3a: Bump malformation**



**Figure 2.3b: Bump bridging**

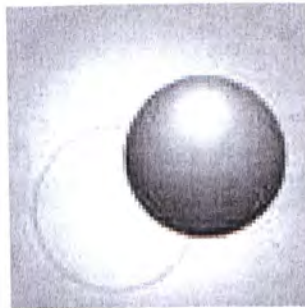


**Figure 2.3c: Bump misplacement**

**Figure 2.3: The common 2D defects of wafer bumps.**

These methods do not require the bumps' three dimensional information, such as height, so we call these kinds of defects- 2D defects.

**3D defects**

During the process of wafer-level packaging production, the main part is to realize the bump-bump connection. If the height of the bump can not meet the requirement, simply understood as not as the same height as the golden bump, that will lead to the whole wafer to be invalid. Thus, the inspection of height of bumps and coplanarity is a must before packaging. In this stage, the general 2D measurement can not get to the destination. We need to apply 3D measurement. However, 3D measurement methodology is somewhat less standard than 2D across the industry [6]. The problems of height measurement are that the reflectance of the wafer surface varies widely, and high-speed measurement is necessary. Normally, the darkest area and brightest area differ 20 times in brightness. In the measurement, all bumps on the wafer must be measured, and the height acquisition time should be less than 10 seconds, taking into account the image processing time.



**Figure 2.4: The coplanarity requirement of the wafer bumps**

## **2.3 Traditional Methods for Bump Inspection**

At present, three inspection technologies predominant: laser scanning and image analysis, confocal microscopy, and Moiré interferometry [7]. All three methods require the use of moving parts, stringent light projection system, and exact mirror and lenses for scanning and focusing which are all costly.

August Technology uses a confocal sensor in their 3D system that compromises on speed in exchange for better accuracy. ICOS uses stereo imaging that does not yet give good 3D profile information. RVSI has better 3D measurement techniques but not as good defect detection and classification.

### **Laser Scan and Image Analysis**

This technique relies on sensors to measure light reflected off a target onto either a pixelized array detector or a position-sensing detector [8]. The laser diode for the sensor projects a beam of light onto the target. The light-sensitive detector built into the sensor receives some of the reflected light and records the position of the reflected beam, along with a measurement of height. As the target (or the sensor) moves to another image point on the component, the position of the reflected light beam changes, and new data (height and position) are recorded as a delta from the previous position.

The technology is somewhat limited for in-tray inspection, because the components need to be perfectly aligned for the laser beam to properly inspect



them. The laser also scans only the areas of the component directly in-line with the path. Those areas between the laser paths assume a comparable surface, which can lead to missed defects. Then too, laser triangulation measures only height (Z axis), and must be combined with an X-Y mechanism to obtain 3D or 2D data. As the target or sensor moves, the spinning mirrors and precision drives represent a complex system that can be adversely affected by mechanical wear and other problems.

Finally, the most limiting aspect of laser technology (in addition to speed) is undoubtedly spot size, the diameter of the "spot" made by the laser at the point of contact. If the diameter, for instance, is 30 microns, then the system cannot detect lateral features less than 30 microns. Such a limitation is acceptable for BGAs, but not so for smaller components, such as micro BGAs [9] and flip chips. Lasers [10] are also subject to the "speckle" effect (noise or interference in the image produced by scattering of the reflected beam).

The principle of laser scan [11][12] can be seen in Fig.2.5. The laser referred in this method is like a plane scanning from one side of the bump to the other. During this process, there is camera placed perpendicular to the substrate of the wafer grabbing several images. The more the pictures the camera grabbed, the more information we will get from the images. With these images, the bumps' 3-D information can be got.

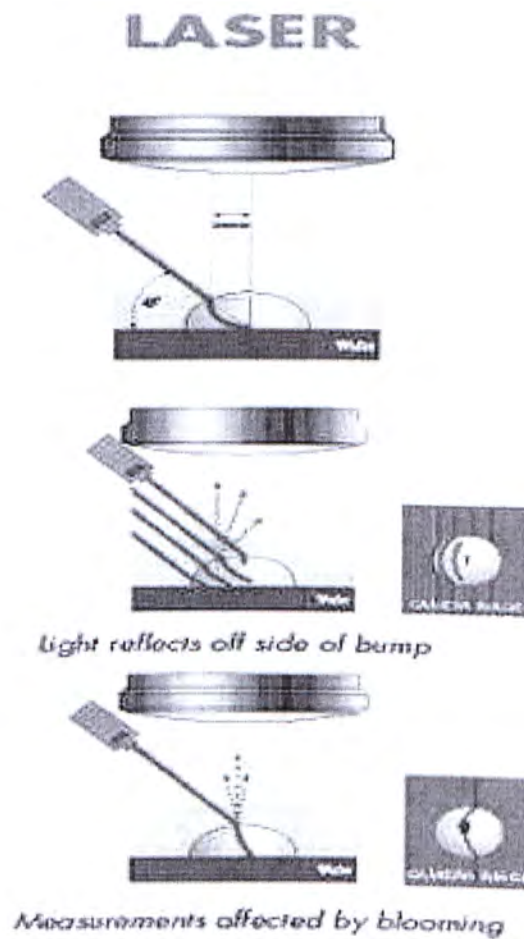


**Figure 2.5: Principle of Laser scan system**

### **Confocal Microscopy**

The process is based on producing a linearly polarized beam using a laser, the beam being transmitted through various optical elements mirrors, lenses, beam splitter, in hole plate, etc. where it impinges a target, such as a solder bump, at a specific and minute location. (The beam at the impingement point on the target



is about a micron in diameter.) The beam is then reflected back, filtered to produce a high signal-to-noise ratio, and passed through the beam splitter [13], where it is deflected at right angles to the path of the transmitted beam and is directed by a turning mirror to a photo detector. The photo detector converts the amount of light into digital output to a computer. The image composed from the various impingement points on the target is subsequently displayed on the computer monitor.

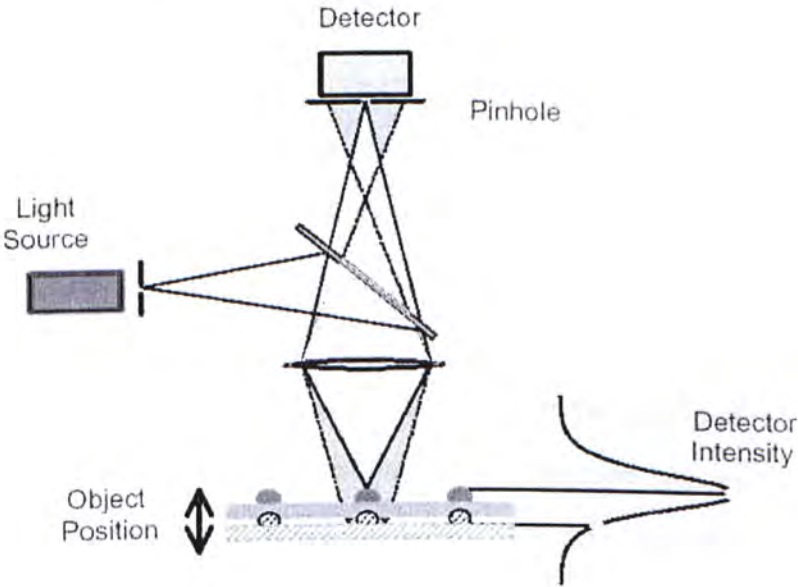


**Figure 2.6: Principle of confocal system**

The method measures the amount of light reflecting directly off the top of any feature on a wafer surface. It correlates the light intensity with the vertical position of the sensor through a relationship defined by the confocal optics. Actual feature height is calculated by comparing the relative height of the

feature to a reference surface selected by the user. The confocal method uses a continuous scanning motion to capture feature height data and its speed is independent of the number of bumps on die or on a wafer.

The problem with confocal imaging equipment, besides the high capital expense, is the extreme degree of alignment that must be maintained in terms of the optics (mirrors, lenses, etc.). Vibration and shock, even through normal conveyor movement, can disturb the alignment and provide erroneous data. Setup time can also be lengthy. In addition, throughput is a major issue. Since confocal [14] [15], imaging is conducted at several Z-locations (at least 5 to 7 layers), inspection speed is greatly reduced. As a result, a sampling alternative is suggested instead of 100 percent inspection of the entire part.

### **Moiré interferometry**

This technology has been employed for many years in 3D profiling of difficult-to-measure parts in various industries other than electronics (e.g., automotive, aeronautics, and manufacturing equipment [16]. The procedure entails: Illuminating a bump with a moire light pattern created by projecting a laser or white light beam through a grid and capturing the resulting image with a CCD (charge coupled device) camera. Moving the light pattern a few microns and capturing another image. Repeat the process for a third time. In each case, light intensity and position readings are measured and processed by software to achieve a profile of the target object.

In recent years, a few companies have tried to develop a Moire Interferometry inspection [17] tool for the electronics manufacturing environment, but have encountered several challenges. One company uses a scanning process, which requires that the component be conveyed in a tray or on tape beneath the camera and laser system, thereby limiting inspection throughput. Scanning speed is said to be 125mm per second.

### **Fast Moiré Interferometry (FMI)**

FMI [18] (fast moire interferometry) is an evolution of the basic moire technology; and as such, it raises moire interferometry to a level where the process is clearly superior to other techniques for inspecting bumped packages. The result is three times the inspection speed of existing moire interferometry systems. Fig.2.7 depicts the configuration for FMI. The features and performance characteristics of FMI inspection [19] technology can be summarized as follows:

FMI uses a single CCD camera, combined with a projector that diffuses a white light pattern on the component or tray of components being inspected through a grating mounted in the projection assembly. The light source provides an intense beam using an optical fiber coupled with an aspherical lens located between the light source and the grating. A grating of light is thus projected onto the component, following the Z-topography of the surface.

The color CCD camera is situated directly above the component at a 90 degree angle to the platform, while the projector is fixed at a 30 degree angle. (The camera and the projector are mounted on the same gantry system.) The high-resolution camera captures the image of the grating projection on the component, and converts the pixel data into digital output. The system captures an entire field of view; therefore, no scanning is required. In fact, the field of view can be scaled up to encompass multiple components simultaneously. Data is thus acquired faster than with any other system on the market.



**Figure 2.7: Configuration of Moire Interferometry**



**Figure 2.8: 3D Z-topography of bare die showing a bump defect**

Unique to FMI is the fact that the grating, which creates the moire pattern on the target, is moved sequentially four times with high precision. As the grating moves, four different images are recorded, along with multiple levels of intensity. Algorithm software then converts the data into 3D and 2D images simultaneously.

FMI incorporates a proprietary methodology-volume pixel acquisition (VPA) [20] which captures X and Y, as well as Z data for each pixel Fig.2.9.

Superior X-Y platform control is achieved through the use of servo motors and encoders. The 2D x-y data depicts such conditions as the presence/absence of bumps, proper fiducial alignment, correct component markings and so on. The captured X, Y, and Z data results in a “pass” or “fail” indication by the system

FMI systems can inspect individual components or multiple components in a tray. When required, a magnetic transfer table is used to move the packages from the tray to the work area.



Using VPA, the volume of solder bumps and balls can be determined. FMI technology can also be employed to inspect the quality of the mold encapsulating both leaded and area array devices and packages.

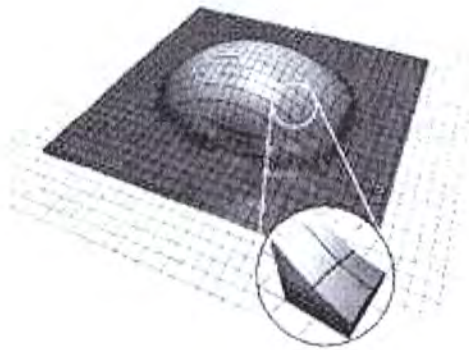


**Figure 2.9: Volume pixel acquisition (VPA) methodology captures X, Y and Z data for each pixel.**

While area array components seldom require interconnect diameters under 10 mils (0.010 in.), FMI systems can inspect bumps and balls as small as 40 microns in height.

Fast moire inspection equipment is available today as fully automated, programmable inline systems for 3D and 2D inspection and as semi-automated batch systems for offline process verification and product development. The equipment can also be designed as a module to be incorporated within other production equipment, such as a system that places solder balls on BGAs (ball grid arrays) or flip chips. The module would enable automatic inspection of the



existence and linear placement of the balls, as well as ball height, volume, and substrate warp.

In addition to packaging, FMI technology offers particular advantages in the 3D inspection of various electronic components, given the superior processing speed and the sub-micron precision achieved. Other applications include inspection of solder paste after stencil printing of circuit boards and inspection of wafer-level packages[21], namely solder bumps on 200mm and 300mm wafers. In the case of both solder paste and wafer bumps, FMI enables in-line line inspection without degrading throughput, though offline batch inspection would be possible as well, depending on the line set-up and requirements of the manufacturer.

In a word, all three methods require the use of moving parts, stringent light projection system, and exact mirror and lenses for scanning and focusing which are all costly. However, in many applications, detailed 3D shape profile of the target surfaces (the bump surfaces in the case of wafer inspection) is not needed. What is needed is to measure whether the bump heights on the whole meet the specifications or not, as well as to identify the individual bumps that are too tall or too short.

This work aims at coming up with a system that does just that, requires an integrated study of an innovative approach in the lighting, optics and image processing that is suitable for development in the academic environment

without going through explicit 3D reconstruction and thus saving operation speed and hardware cost of the whole system.

## Chapter 3

### BIPLANAR DISPARITY METHOD

#### 3.1 Problem Nature

We now understand the followings:

- The bump is ball shape with diameter tens to hundreds microns, and its surface is textureless and has a mirror-like reflective property. While the substrate is usually lambertian surface with diffuse reflectivity and has some texture on it as shown in Fig. 3.1 and 3.2.
- Most of the bumps are of the same height, say, the average height, which is usually the standard height, while some of them may deviate the average height, which are considered as outliers, and result in bad wafer. And in some cases, although rarely, the average height may deviate the standard. This may be caused by parameter mistake in fabrication, and will result in bad wafer too. Both of the defects should be detected in bump height inspection.

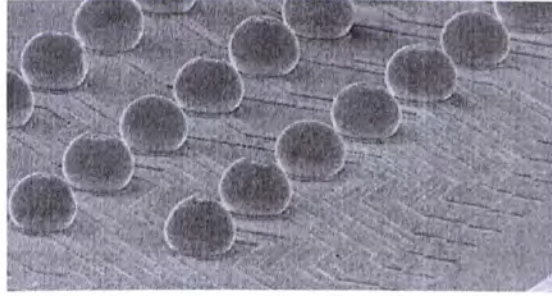


**Figure 3.1: Image of the bump grid array**

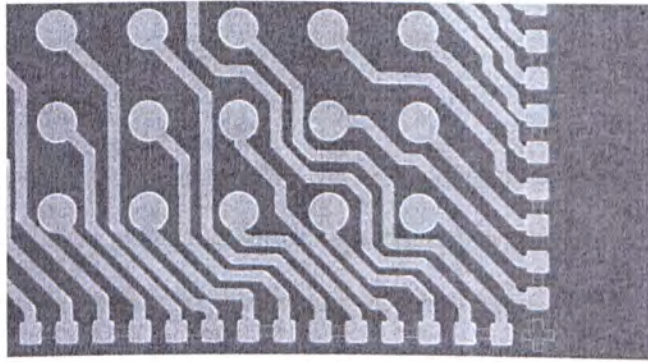


**Figure 3.2: Image of the substrate**

Our bump height inspection is based on above prerequisite, which is also the case in real industry, and the objective is to check whether the heights of the bumps meet the standard, without considering the 2D defects, such as bump misplacement (offset), or other 3D defects such as bump shape malformation or bump bridging, for illustration:

- The inspection should not be about the distance of the bump peaks from a camera, but about the heights of all the bumps on the substrate, i.e.,

about the distance bumps' peaks from their bottoms, to justify whether they are all standard or not.

- Isolated bumps whose heights deviate too much from the average height, i.e., the bumps too tall or too short beyond the tolerance, should be identified, which we mark as defect A in the following parts. The average height will also be checked then, to see whether the bumps is globally too tall or too short, which we mark as defect B in the following parts.
- The method should be invariant with limited rigid transformation of the wafer, such as global transformation and rotation, which is caused by the feed in system and other disturbance in inspecting process.

As achieving these objectives, we also have following desires for practical consideration of efficiency, robustness, and simplicity of implement:

- Parallel operation to examine multiple bumps at the same time, so as to get high speed in and output.
- Less moving parts in hardware setting, so as to be fast, to reduce positioning uncertainty or the need of high-cost positioning stage, and to reduce the need of frequent positioning calibration that would require the inspection system to be paused.



- Avoid using additional markers on wafer, for image registration, so as to reduce additional uncertainty to the problem.

## 3.2 System Overview

As we introduced in chapter 2, there have been a few methods developed for the bump height inspection, but they all require explicit 3D reconstruction which is an expensive process especially for dimensions of such a miniature scale. So here we focus our intension on the HEIGHT, that is, the distance from the TOP POINTS of the bumps to the substrate. As we stated in previous part, most of the bumps are of the same size, which means their top points will be contained in a certain plane, the top plane denoted as  $\Pi_t$ . And the substrate will induce another plane, the substrate plane denoted as  $\Pi_b$ . Then the problem of bump height inspection is converted to the problem of finding the distance between these two planes. The idea is illustrated in Fig.3.3. Homography matrix is chosen to describe the planes, and the relation between homography matrices of the planes and the distance between them are deduced in the following parts. A matrix called Biplanar Disparity matrix is calculated from the homography matrices and the camera parameter, to reveal the distance information of the planes, and our method is so named Biplanar Dispartiy Method (BDM).



**Figure 3.3: The two planes reveal the bump height information**

Traditionally, the reflective property of the bump surface and substrate surface will cause great difficulty in inspection, since the mirror-like reflectivity makes it hard to find features on the bump surface and the significant difference of the reflectivity between the bump surface and the substrate surface will cause conflict in illumination setting. But now here we just utilize this property to grab correspondences on the textureless bump surface by a specially designed imaging setup depicted in Fig.3.4 and to get access to the two planes we concerned.

There are two cameras in the system, showed in blue and red color respectively for discrimination in the figure. One is fixed right above the inspected wafer (the red one), and the other on the side, with a certain  $\mathbf{R}$  and  $\mathbf{t}$  to the red one (about 15 to 30 degree in rotation). Both are focusing on the same wafer to be inspected, but each one with its own parallel illumination, indicated in the same color as the camera. Illumination for the center camera projected from the same direction as the camera, that is, perpendicular to the inspected wafer. While illumination for the side camera projected just from the symmetrical direction to the camera. In practical, we design fine calibration to position the light source and cameras to make sure that (the center camera and its illumination) and (the

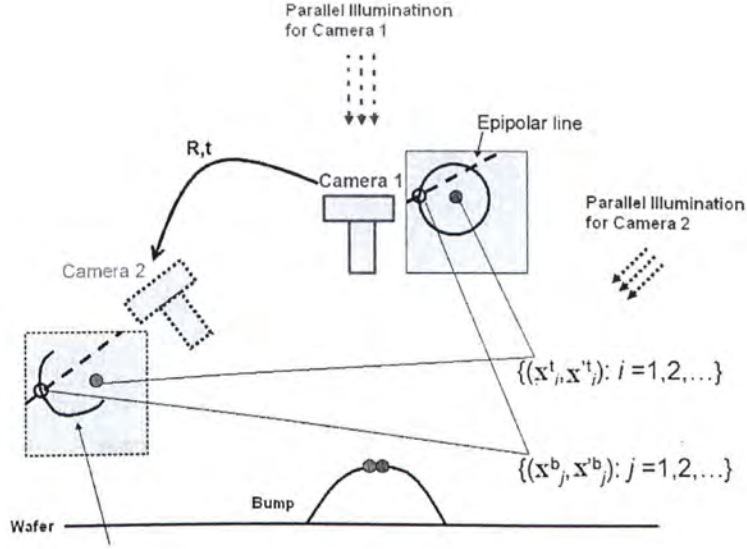


**Figure 3.4: Imaging setting of the Biplanar Disparity Method (BDM)**

side camera and its illumination) have the same angle bisector orientation with respect to the inspected wafer. The calibration process will be explained in the experiment part.

Now that we understand the ball shape and the mirror-like reflectivity of the bump surface, the camera will only capture the light reflected by the points at the top area under this imaging setting, and the TOP POINTS of the bumps will cast the brightest points in the images, while the other area on the bump surface will be dark in the image, as illustrated in Fig.3.5. The correspondences on the top plane is simultaneously obtained by matching the brightest points in the center image and side image, recorded as  $\{(x_i^t, x_i^{t'}), i = 1, 2, \dots\}$ . The correspondences on the substrate, recorded as  $\{(x_j^b, x_j^{b'}), j = 1, 2, \dots\}$ , could be

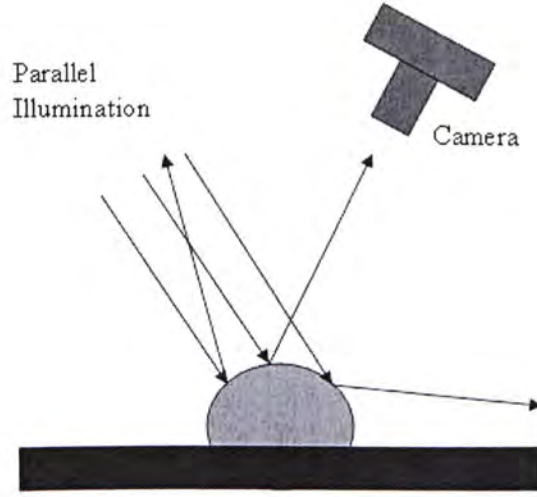


**Figure 3.5: The top points will cast the brightest points in the image**

found by normal feature detection and stereo matching method [22] [23], for it is a Lambertian surface with texture as shown in Fig.3.2.

There are some points we should note:

- Exploiting the mirror-like reflectivity of the bumps, 2 cameras and 2 parallel light sources of different colors, if properly positioned in 3D (so that in 3D the red dot and the blue dot coincide) as illustrated in Fig.3.4, and coupled with the use of the epipolar constraint (which is captured by a  $3 \times 3$  matrix  $\mathbf{F}$  named the Fundamental matrix), could allow image point correspondences  $\{(\mathbf{x}'_i, \mathbf{x}''_i) : i = 1, 2, \dots\}$  over the bump peaks, and  $\{(\mathbf{x}^b_j, \mathbf{x}^{b'}_j) : j = 1, 2, \dots\}$  over the bump bottoms, to be available over a number of bumps in the wafer.

- Such 2 sets of correspondences would allow the two homographies  $\mathbf{H}_l$  and  $\mathbf{H}_h$ , which are for the planes  $\Pi_l$  and  $\Pi_h$  respectively, to be estimated through the use of the property

$$\begin{bmatrix} \mathbf{x}'_i \\ 1 \end{bmatrix} \cong \mathbf{H}_l \begin{bmatrix} \mathbf{x}_i \\ 1 \end{bmatrix} \quad (3.1)$$

for all  $i$ , and

$$\begin{bmatrix} \mathbf{x}'^{hb}_j \\ 1 \end{bmatrix} \cong \mathbf{H}_h \begin{bmatrix} \mathbf{x}_j \\ 1 \end{bmatrix} \quad (3.2)$$

for all  $j$ .

- Isolated bumps whose heights deviate too much from the majority value could be identified with robust estimation of  $\mathbf{H}_l$  and  $\mathbf{H}_h$ .
- The use of homography makes the whole system be sensitive not to the individual 2D positions of the bumps but the overall positions of planes  $\Pi_l$  and  $\Pi_h$ . Because we only focus on the global height of bump, not the individual position.

Then, if we could come up with an invariance about the difference of planes  $\Pi_l$  and  $\Pi_h$ , which should be more or less preserved (to the limit of a threshold) across wafers, our problem can be solved.



### 3.3 Biplanar Disparity Matrix D

With the above, suppose  $\hat{\mathbf{n}}$  is the unit surface normal vector of plane  $\Pi$  with reference to the camera coordinate frame, and  $d$  is the perpendicular distance of the plane to the camera center. Notice that  $(\hat{\mathbf{n}}, d)$  is one precise way of describing a plane in 3D. An variance about the difference of the two planes  $\Pi_b$  and  $\Pi_s$  could be  $(\frac{\hat{\mathbf{n}}_t}{d_t} - \frac{\hat{\mathbf{n}}_b}{d_b})$ . The idea is illustrated in Fig.3.6. The question is, how could we go from  $\mathbf{H}_t$  and  $\mathbf{H}_b$ , that could be estimated as outlined above, to a measure of this invariance for each incoming wafer and compare the measure with that of the reference wafer?

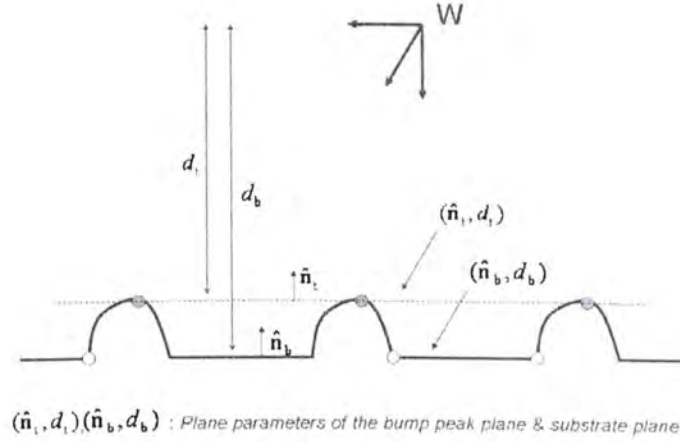


**Figure 3.6: The idea to get the height information by plane parameters**

Suppose we have access to 2 images  $I$  and  $I'$  of the same plane  $\Pi$ , and the camera intrinsic parameter matrices  $\mathbf{A}$  and  $\mathbf{A}'$  of the 2 cameras. Let  $\mathbf{P}$  be the position vector of any 3D point on  $\Pi$ , with respect to the camera coordinate frame of  $I$  (camera 1). Let  $\mathbf{P}'$  be the corresponding position vector from the camera coordinate frame of  $I'$  (camera 2). Then  $\hat{\mathbf{n}} \cdot (\mathbf{P} - \mathbf{P}_0) = 0$  where  $\mathbf{P}_0$  is the position of a fixed point on  $\Pi$ . For a plane  $\Pi$ , the plane normal is defined as  $\frac{\hat{\mathbf{n}}}{d}$ ,

and for all the points  $\mathbf{P} \in \pi$ , we have  $\frac{\hat{\mathbf{n}}^T}{d} \bullet \mathbf{P} = 1$  [24].

The above could be simplified to

$$\hat{\mathbf{n}} \cdot \mathbf{P} = \hat{\mathbf{n}} \cdot \mathbf{P}_0 = d \quad (3.3)$$

We also have

$$\mathbf{P} = \mathbf{R}\mathbf{P}' + \mathbf{t} \quad (3.4)$$

where  $\mathbf{R}$  and  $\mathbf{t}$  are the rotation and translation matrices between the two cameras.

Eqt. (3.3) and (3.4) together imply

$$\mathbf{P}' = \mathbf{R}^{-1}\mathbf{P} - \mathbf{R}^{-1}\mathbf{t}\left(\frac{1}{d}\hat{\mathbf{n}}^T\mathbf{P}\right) \quad (3.5)$$

or simply

$$\mathbf{P}' = \mathbf{R}^{-1}\left(\mathbf{I} - \mathbf{t}\frac{\hat{\mathbf{n}}^T}{d}\right)\mathbf{P} \quad (3.6)$$

Since the corresponding image positions  $(\mathbf{p}, \mathbf{p}')$  in  $I$  and  $I'$  have the properties

$\mathbf{p} = (x, y, 1)^T \cong \mathbf{A}[\mathbf{I}, 0][\mathbf{P}^T, 1]^T \cong \mathbf{A}\mathbf{I}\mathbf{P} \cong \mathbf{A}\mathbf{P}$  and  $\mathbf{p}' = (x', y', 1)^T \cong \mathbf{A}'\mathbf{P}'$ , we have

$$\mathbf{p}' \cong [\mathbf{A}'\mathbf{R}^{-1}(\mathbf{I} - \mathbf{t}\frac{\mathbf{n}^T}{d})\mathbf{A}^{-1}]\mathbf{p} \quad (3.7)$$

Together with Equations (3.1) and (3.2), the above means:

$$\mathbf{H} \cong \mathbf{A}'\mathbf{R}^{-1}(\mathbf{I} - \mathbf{t}\frac{\hat{\mathbf{n}}^T}{d})\mathbf{A}^{-1} \quad (3.8)$$

Equation (3.8) for a normalized  $\hat{\mathbf{H}}$  could be written as

$\hat{\mathbf{H}} = w\mathbf{A}'\mathbf{R}^{-1}(\mathbf{I} - \mathbf{t}\frac{\hat{\mathbf{n}}^T}{d})\mathbf{A}^{-1}$ , for some unknown  $w$ . The equation could be

simplified to  $[\mathbf{t}]_x \mathbf{R}\mathbf{A}'^{-1} \hat{\mathbf{H}} = w[\mathbf{t}]_x \mathbf{A}^{-1}$ , which could be expressed as

$\mathbf{F}\hat{\mathbf{H}} = w(\mathbf{A}^{-1})^T[\mathbf{t}]_x \mathbf{A}^{-1}$  where  $\mathbf{F} = (\mathbf{A}^{-1})^T[\mathbf{t}]_x \mathbf{R}\mathbf{A}'^{-1}$  is the fundamental matrix of

the camera pair [25], and  $[\mathbf{t}]_x$  is the  $3 \times 3$  skew-symmetric matrix corresponding

to the translation vector  $\mathbf{t}$ . For  $\mathbf{t} = (t_1, t_2, t_3)^T$ , the corresponding skew-

symmetric matrix is:

$$[\mathbf{t}]_x = \begin{bmatrix} 0 & -t_3 & t_2 \\ t_3 & 0 & -t_1 \\ -t_2 & t_1 & 0 \end{bmatrix} \quad (3.9)$$

In other words, given unit-norm  $\hat{\mathbf{H}}$  and unit-norm  $\hat{\mathbf{F}}$ , the unknown scale  $w$

could be determined in terms of a particular scalar  $\alpha$  from the Eq. (3.10).

$$\hat{\mathbf{F}}\hat{\mathbf{H}} = \frac{w}{\alpha}(\mathbf{A}^{-1})^T[\mathbf{t}]_x\mathbf{A}^{-1} \quad (3.10)$$

where  $\alpha$  is a constant related to the values of  $\mathbf{A}$ ,  $\mathbf{A}'$ ,  $\mathbf{R}$ , and  $\mathbf{t}$ , not  $\Pi_t$  and  $\Pi_b$ .

Suppose  $\hat{\mathbf{H}}_t$  and  $\hat{\mathbf{H}}_b$  are the unit-norm  $\mathbf{H}_t$  and  $\mathbf{H}_b$  for planes  $\Pi_t$  and  $\Pi_b$  respectively. And  $w_t$  and  $w_b$  are the unknown scales in Equation (3.10) for  $\hat{\mathbf{H}}_t$  and  $\hat{\mathbf{H}}_b$ .  $\frac{w_t}{\alpha}$  and  $\frac{w_b}{\alpha}$ , for some  $\alpha$ , could be determined respectively from  $\hat{\mathbf{H}}_t$ ,  $\hat{\mathbf{H}}_b$ , and  $\hat{\mathbf{F}}$  through the use of Equation (3.10).

Since

$$\hat{\mathbf{H}}_b = w_b\mathbf{A}'\mathbf{R}^{-1}(\mathbf{I} - \mathbf{t}\frac{\hat{\mathbf{n}}_b^T}{d_b})\mathbf{A}^{-1} \quad (3.11)$$

we have

$$(\hat{\mathbf{H}}_t/\frac{w_t}{\alpha} - \hat{\mathbf{H}}_b/\frac{w_b}{\alpha}) = -\alpha\mathbf{A}'\mathbf{R}^{-1}\mathbf{t}(\frac{\hat{\mathbf{n}}_t^T}{d_t} - \frac{\hat{\mathbf{n}}_b^T}{d_b})\mathbf{A}^{-1} \quad (3.12)$$

which is about a fixed-value transformation (for fixed  $\mathbf{A}$ ,  $\mathbf{A}'$ ,  $\mathbf{R}$ ,  $\mathbf{t}$ ) of  $(\frac{\hat{\mathbf{n}}_t}{d_t} - \frac{\hat{\mathbf{n}}_b}{d_b})$ .

In other words, an invariance of the difference of the planes  $\Pi_t$  and  $\Pi_b$  is:

$$\mathbf{D} = \frac{\hat{\mathbf{H}}_t}{\frac{w_t}{\alpha}} - \frac{\hat{\mathbf{H}}_b}{\frac{w_b}{\alpha}} \quad (3.13)$$

What we should notice here is:

- 1) When the camera system is fixed, that is, the parameters  $\mathbf{A}$ ,  $\mathbf{A}'$ ,  $\mathbf{R}$ ,  $\mathbf{t}$  are fixed, the matrix  $\mathbf{D}$  will be fully determined by  $(\frac{\hat{\mathbf{n}}_l}{d_l} - \frac{\hat{\mathbf{n}}_b}{d_b})$ , which represents the difference vector of the two planes  $\Pi_l$  and  $\Pi_b$ . So the change of the entries in matrix  $\mathbf{D}$ , will reflect the change in the separation of these two planes, that is, the change in the bump heights.
- 2) Since the subtraction operation is not a one-to-one imaging, the original value of the  $\frac{\hat{\mathbf{n}}_l}{d_l}$  and  $\frac{\hat{\mathbf{n}}_b}{d_b}$  has been lost during the subtraction, but only their difference is preserved. This means the matrix  $\mathbf{D}$  invariant to the exact position of the planes, which makes our algorithm robust to the global disturbance of the wafer, such as global transformation, rotation or tilting.
- 3) Normally the output of the real inspection is to give a qualitative analysis on whether the inspected wafer is to be rejected or accepted. So we will not try to recover the exact distance of the two planes from  $(\frac{\hat{\mathbf{n}}_l}{d_l} - \frac{\hat{\mathbf{n}}_b}{d_b})$ , but only to get the disparity matrix  $\mathbf{D}$  corresponding to the  $(\frac{\hat{\mathbf{n}}_l}{d_l} - \frac{\hat{\mathbf{n}}_b}{d_b})$  of each wafer, and then compare it to the standard  $\mathbf{D}$  to see whether it meets the requirement.



Such a disparity matrix  $\mathbf{D}$  encodes the difference between two planes: the plane that contains the peaks of the bumps, and the plane that contains the bottom of the bumps. It is invariant to global transformation of the wafer, but variant to relative transformation between the two planes, and is thus a measure we could use to decide if a wafer has bump heights that meet the specifications or not.

To investigate how the item  $(\frac{\hat{\mathbf{n}}_t}{d_t} - \frac{\hat{\mathbf{n}}_b}{d_b})$  influences the entries in  $\mathbf{D}$ , we make the following notations:

$$(\frac{\hat{\mathbf{n}}_t}{d_t} - \frac{\hat{\mathbf{n}}_b}{d_b}) = (x, y, z) \quad (3.14)$$

Here  $x, y, z$  are unknown values revealing the bump heights information.

$$-\alpha \mathbf{A}' \mathbf{R}^{-1} \mathbf{t} = \begin{pmatrix} a \\ b \\ c \end{pmatrix} \quad (3.15)$$

$$\mathbf{A}^{-1} = \begin{pmatrix} p_{11} & p_{12} & p_{13} \\ p_{21} & p_{22} & p_{23} \\ p_{31} & p_{32} & p_{33} \end{pmatrix} \quad (3.16)$$

The entries  $a, b, c, p$  are all considered known values once the imaging system is fixed and calibrated. Then the matrix  $\mathbf{D}$  can be written in:

$$\begin{aligned}
\mathbf{D} &= \begin{pmatrix} a \\ b \\ c \end{pmatrix} \begin{pmatrix} x & y & z \end{pmatrix} \begin{pmatrix} p_{11} & p_{12} & p_{13} \\ p_{21} & p_{22} & p_{23} \\ p_{31} & p_{32} & p_{33} \end{pmatrix} \\
&= \begin{pmatrix} ap_{11}x + ap_{21}y + ap_{31}z & ap_{12}x + ap_{22}y + ap_{32}z & ap_{13}x + ap_{23}y + ap_{33}z \\ bp_{11}x + bp_{21}y + bp_{31}z & bp_{12}x + bp_{22}y + bp_{32}z & bp_{13}x + bp_{23}y + bp_{33}z \\ cp_{11}x + cp_{21}y + cp_{31}z & cp_{12}x + cp_{22}y + cp_{32}z & cp_{13}x + cp_{23}y + cp_{33}z \end{pmatrix} \quad (3.17)
\end{aligned}$$

We see that every entry of  $\mathbf{D}$  is linearly coupled with the all three unknowns  $x$ ,  $y$ ,  $z$ , so the norm of  $\mathbf{D}$  will directly reflect the change in the bump height information.

### 3.4 Planar Homography

#### 3.4.1 Planar Homography

A planar homography is a projective transformations that map points from one plane to another plane (for example the transformation mapping points in a planar surface in the world to the image plane). It represents a collineation between a world plane and its perspective image [26]. The easiest way to see it is to choose the world coordinate system such that the plane has equation  $z = 0$ . Expanding the projection equation gives:

$$\begin{pmatrix} u \\ v \\ 1 \end{pmatrix} \cong \begin{pmatrix} p_{11} & p_{12} & p_{13} & p_{14} \\ p_{21} & p_{22} & p_{23} & p_{24} \\ p_{31} & p_{32} & p_{33} & p_{34} \end{pmatrix} \begin{pmatrix} x \\ y \\ 0 \\ 1 \end{pmatrix} \cong \begin{pmatrix} p_{11} & p_{12} & p_{14} \\ p_{21} & p_{22} & p_{24} \\ p_{31} & p_{32} & p_{34} \end{pmatrix} \begin{pmatrix} x \\ y \\ 1 \end{pmatrix} \cong \mathbf{H} \begin{pmatrix} x \\ y \\ 1 \end{pmatrix} \quad (3.18)$$

Where  $\mathbf{H}$  is a 3 by 3 nonsingular matrix. Fig.3.7 illustrates the geometry involved in this process.

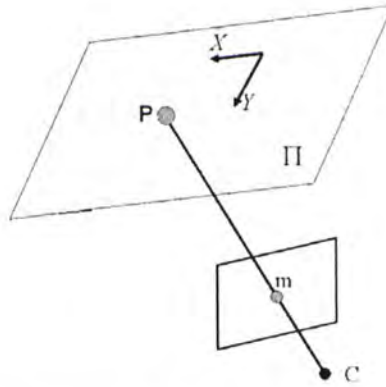


**Figure 3.7: Homography between a 3D plane and its image**

Now consider the problem of determining the homography that maps points in one image to the corresponding points in a second image. Assuming that we can identify corresponding points in both images (let's say, by detecting and matching interest points), such a homography exists and can be computed, consider the homography  $\mathbf{H}_l$  mapping points on a plane to image points on the left side image:

$$\mathbf{x}_{l,i} \cong \mathbf{H}_l \cdot \mathbf{q}_i \quad (3.19)$$

Where  $\mathbf{q}_l = (x, y, 1)^T$  is a point on some plane  $\pi$ , and  $\mathbf{x}_{l,j} = (u_l, v_l, 1)^T$  its projection onto the left image. In a similar fashion, consider the homography  $\mathbf{H}_r$  that maps points on  $\pi$  to image points on the right side image:

$$\mathbf{x}_{r,j} \cong \mathbf{H}_r \cdot \mathbf{q}_l \quad (3.20)$$

Substituting (3.20) in (3.19) we have:

$$\mathbf{x}_{l,j} \cong \mathbf{H}_l \cdot \mathbf{H}_r^{-1} \cdot \mathbf{x}_{r,j} \cong \mathbf{H} \cdot \mathbf{x}_{r,j} \quad (3.21)$$

Where  $\mathbf{H} = \mathbf{H}_l \cdot \mathbf{H}_r^{-1}$  is the homography that maps points on the right side image to points on the left side image. Notice that we can do this without ever knowing the location of the points  $\mathbf{q}_l$ . The homography induced by a plane is unique up to a scale factor and is determined by 8 parameters or degrees of freedom. The homography depends on the intrinsic and extrinsic parameters of

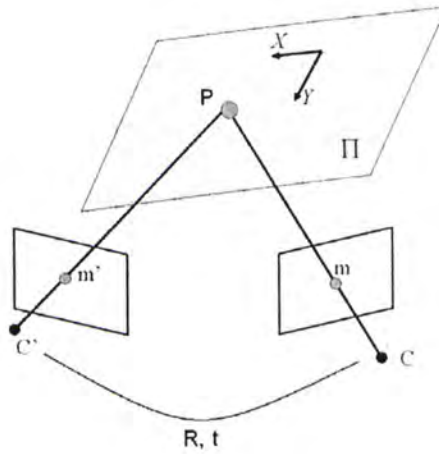


Figure 3.8: Homography between the two images of a 3D plane

the cameras used for the two views and the parameters of the 3D plane. Fig.3.8 illustrates the geometry involved in this process.

Homographies can be applied to many problems in computer vision including stereo reconstruction, image mosaics, and applications using perspective geometry [27][28].

In our Biplanar Disparity Method, we use homography as a description of the planes we concerned, the top plane  $\Pi_t$  and the substrate plane  $\Pi_b$ . It could be constructed directly from the correspondences on the two images and is taken as a global parameter of the plane to reveal the 3D position of the plane but not the individual points on the plane, so make the parallel inspection of massive bumps possible.

### 3.4.2 Homography Estimation

Planar homography between two views can be determined by finding sufficient constraints to fix the (up to) 8 degrees of freedom of the relation [29]. Homography can be estimated from the matching of 4 points or lines or their combinations in general positions in two views. Each matching pair gives two constraints and fixes two degrees of freedom. In practice, robust statistical techniques are employed on a large number of matching points or lines after normalizing the data to reduce the adverse effects of noise, quantization, etc [30]. The degrees of freedom can be fixed by matching other parametric and non-parametric curves or contours in the images. Other gross properties in the



image such as texture can also be used to compute the planar homography between two views [31][32].

In our method, we use the point correspondences for homography estimation. Direct linear transformation [33] is chosen for its robustness and efficiency and Singular Value Decomposition (SVD) [34][35] is used for matrix analysis. The DLT (Direct Linear Transformation) algorithm utilizes the point correspondences for homography estimation, without requiring the epipolar geometry as a precondition or using other high order curves, and could avoid the compounding of the uncertainty in the estimation of these primary structures before computing the homography. And it could be easily implemented by SVD analysis.

Some individual bumps which are too short or tall are considered as outliers. The top points of the outliers will deviate too much from the bump plane and should be picked out during the homography estimation process. So robust estimation method [36] is utilized to classify the inliers and outliers. Then we could estimate the homography with the inliers by DLT. In our real data experiment, since the number of outliers is tend to be big due to the erosion of the bump surface, RANSAC is chosen for its good performance in dealing with big portion outliers case.

### Direct Linear Transformation (DLT) using point correspondences

The equation  $\mathbf{x}' = \mathbf{H}\mathbf{x}$  may be expressed in terms of the vector cross product as

$\mathbf{x}' \times \mathbf{H}\mathbf{x} = \mathbf{0}$ . If the  $j$ -th row of the matrix  $\mathbf{H}$  is denoted by  $\mathbf{h}^{jT}$ , we have

$$\mathbf{H}\mathbf{x}_i = \begin{pmatrix} \mathbf{h}^{1T} \mathbf{x}_i \\ \mathbf{h}^{2T} \mathbf{x}_i \\ \mathbf{h}^{3T} \mathbf{x}_i \end{pmatrix} \quad (3.22)$$

Writing  $\mathbf{x}'_i = (x'_i, y'_i, w'_i)^T$ , the cross product can be given explicitly as

$$\mathbf{x}'_i \times \mathbf{H}\mathbf{x}_i = \begin{pmatrix} y'_i \mathbf{h}^{3T} \mathbf{x}_i - w'_i \mathbf{h}^{2T} \mathbf{x}_i \\ w'_i \mathbf{h}^{1T} \mathbf{x}_i - x'_i \mathbf{h}^{3T} \mathbf{x}_i \\ x'_i \mathbf{h}^{2T} \mathbf{x}_i - y'_i \mathbf{h}^{1T} \mathbf{x}_i \end{pmatrix} \quad (3.23)$$

This can be rewritten in the form

$$\begin{bmatrix} \mathbf{0}^T & -w'_i \mathbf{x}_i^T & y'_i \mathbf{x}_i^T \\ w'_i \mathbf{x}_i^T & \mathbf{0}^T & -x'_i \mathbf{x}_i^T \\ -y'_i \mathbf{x}_i^T & x'_i \mathbf{x}_i^T & \mathbf{0}^T \end{bmatrix} \begin{bmatrix} \mathbf{h}^1 \\ \mathbf{h}^2 \\ \mathbf{h}^3 \end{bmatrix} = \mathbf{0} \quad (3.24)$$

These equations have the form  $\mathbf{L}_i \mathbf{h} = \mathbf{0}$ , where  $\mathbf{L}_i$  is a 3 by 9 matrix, and let

$\mathbf{h} = (\mathbf{h}^{1T} \quad \mathbf{h}^{2T} \quad \mathbf{h}^{3T})^T$ . Although Equation (3.24) contains three equations, only

two of them are linearly independent. Thus each point correspondence gives

two equations in the entries of  $\mathbf{H}$ . The set of equations can be written as

$$\begin{bmatrix} \mathbf{0}^T & -w_i' \mathbf{x}_i'^T & y_i' \mathbf{x}_i'^T \\ w_i' \mathbf{x}_i'^T & \mathbf{0}^T & -x_i' \mathbf{x}_i'^T \end{bmatrix} \begin{bmatrix} \mathbf{h}^1 \\ \mathbf{h}^2 \\ \mathbf{h}^3 \end{bmatrix} = \mathbf{0} \quad (3.25)$$

Given a set of four point correspondences from the plane, a set of equations  $\mathbf{Lh} = \mathbf{0}$  is obtained, where  $\mathbf{L}$  is the matrix obtained by stacking the rows of  $\mathbf{L}_i$  contributed from each correspondence and  $\mathbf{h}$  is the vector of unknown entries of  $\mathbf{H}$ .

In practice, the extracted image points do not satisfy the relation  $\mathbf{x}' = \mathbf{Hx}$  because of noise in the extracted image points. Let us assume that  $\mathbf{x}'_i$  is corrupted by Gaussian noise with mean 0 and covariance matrix  $\mathbf{V}_x$ . Given  $n$  points, Eqt. (3.25) can be written in matrix equation as  $\mathbf{Lh} = \mathbf{0}$ , where  $\mathbf{L}$  is a  $2n \times 9$  matrix. We seek a non-zero solution  $\mathbf{h}$  that minimizes a suitable cost function subject to the constraint  $\|\mathbf{h}\| = 1$ . This is identical to the problem of finding the minimum of the quotient  $\|\mathbf{Lh}\|/\|\mathbf{h}\|$ . The solution is the (unit) eigenvector of  $\mathbf{L}^T \mathbf{L}$  with the least eigenvalue. Equivalently, the solution is the right singular vector associated with the smallest singular value of  $\mathbf{L}$ .

In  $\mathbf{L}$ , some elements are constant 1, some are in pixels, some are in world coordinates, and some are multiplication of both. This makes  $\mathbf{L}$  poorly conditioned numerically. Much better results can be obtained by performing a simple data normalization, prior to running the above procedure. The procedure is suggested as follows.

### Algorithm 3.1 DLT

Goal: Given  $n \geq 4$  2D to 2D point correspondences  $\mathbf{x}_i \leftrightarrow \mathbf{x}'_i$ , determine the 2D homography matrix  $\mathbf{H}$  such that  $\mathbf{x}'_i \leftrightarrow \mathbf{H}\mathbf{x}_i$ .

Algorithm:

1. For each correspondence  $\mathbf{x}_i \leftrightarrow \mathbf{x}'_i$  compute  $\mathbf{L}_i$ . Usually only two first rows needed.
  2. Assemble  $n \times 9$  matrices  $\mathbf{L}_i$  into a single  $n \times 9$  matrix  $\mathbf{L}$ .
  3. Obtain SVD of  $\mathbf{L}$  as  $\mathbf{UDV}^T$ , where  $\mathbf{U}$  and  $\mathbf{V}$  are orthogonal matrices, and  $\mathbf{D}$  is a diagonal matrix with non-negative entries arranged in descending order down the diagonal. Then  $\mathbf{h}$  is last column of  $\mathbf{V}$ .
  4. Determine  $\mathbf{H}$  from  $\mathbf{h}$ .
    - i Transform the image coordinates according to the transformations  $\tilde{\mathbf{x}}_i = \mathbf{T}\mathbf{x}_i$  and  $\tilde{\mathbf{x}}'_i = \mathbf{T}'\mathbf{x}'_i$ .
    - ii Find the transformation  $\tilde{\mathbf{H}}$  from the correspondences  $\tilde{\mathbf{x}}_i \leftrightarrow \tilde{\mathbf{x}}'_i$ .
    - iii Set  $\mathbf{H} = \mathbf{T}'\tilde{\mathbf{H}}\mathbf{T}$ .
- 

Hartley shows that data normalization gives dramatically better results and hence should be considered as an essential step in the algorithm [38]. One of the commonly used transformation is to translate the points so that their centroid is at the origin and the points are scaled such that the average distance from the origin is equal to  $\sqrt{2}$ .

### **Robust Estimation using RANSAC [39]**

So far it was assumed that the only source of error in the set of correspondences,  $\mathbf{x}_i \leftrightarrow \mathbf{x}'_i$ , is in the measurement of positions. In practical situations this assumption is usually not valid because correspondences are computed automatically and are often mismatched. The mismatched points can be considered as outliers to a Gaussian distribution that explains the error in measurements. These outliers can severely disturb the estimated homography and should be identified. The goal then is to determine a set of inliers from the presented correspondences so that the homography can be estimated in an optimal manner from these inliers using the algorithm described in the previous section. This is robust estimation since the estimation is robust or tolerant to outliers, i.e., measurements following a different, and possibly unmodelled, error distribution.

The RANSAC algorithm [40] can be applied to the putative correspondences to estimate the homography and the (inlier) correspondences which are consistent with this estimate. The sample size is four, since four correspondences determine a homography. The number of samples is set adaptively as the proportion of outliers is determined from each consensus state.

#### **Algorithm 3.2 RANSAC**

Goal: Compute the homography between the two images given a set of candidate matches.

Algorithm:

1. Select four points from the set of candidate matches, and compute homography.
2. Select all the pairs which agree with the homography. A pair  $(\mathbf{x}; \mathbf{x}')$ , is considered to agree with a homography  $H$ , if  $dH(H\mathbf{x}, \mathbf{x}') < t$ , for some threshold



$t$  as the distance threshold between data point and the model used to decide whether a point is an inlier or not, and  $d(.)$  is the Euclidean distance between two points.

3. Repeat steps 1 and 2 until a sufficient number of pairs are consistent with the computed homography.

4. Recompute the homography using all consistent correspondences.

---

There are some important issues in robust estimation using the above procedure [41]. The distance threshold  $t$  should be chosen, such that the point is an inlier with a probability  $\beta$ . This calculation requires known probability distribution for the distance of an inlier from the model. In practice, the distance threshold  $t$  is chosen empirically so that the probability  $\beta$  that the point is an inlier is high, such as, 0.95. Secondly, trying every possible sample may be prohibitively expensive. Instead a large number of samples are used so that at least one of the random samples of 4 points is free from outliers with a high probability, such as, 0.99. Another rule of thumb employed is to terminate the iterations if the size of the consensus set  $T$  is similar to the number of inliers believed to be in the data set. In our experiments we empirically set the inliers as 85%. Given the assumed proportion of outliers, we can use  $T = (1 - t)n$  for  $n$  data points.

## 3.5 Harris Corner Detector

### A. Harris corner detector

Harris Corner Detector was developed in [42] by Harris, C. and Stephens, M (1988). It provides good repeatability under varying rotation and illumination,

and is widely used in stereo matching and image data retrieval. The problem of detecting corners was analyzed in terms of the local image intensity autocorrelation function. A version of the intensity spatial change function for a small shift ( $u, v$ ) can be written as follows:

$$E(u, v) = \sum_{x, y} w(x, y) [I(x + u, x + v) - I(x, y)]^2 = [u, v] M \begin{bmatrix} u \\ v \end{bmatrix} \quad (3.26)$$

$$M = \sum_{x, y} w(x, y) \begin{bmatrix} I_x^2 & I_x I_y \\ I_x I_y & I_y^2 \end{bmatrix} \quad (3.27)$$

$I(x, y)$  denotes the image intensity.  $E(u, v)$  is the average change of image intensity.  $w(x, y)$  is a smoothing window. Let  $\lambda_1$  and  $\lambda_2$  be the eigenvalues of matrix  $M$ . Then **HCD** is given by the following operator where a large value of  $R$  signals the presence of corner in Equation (3.28).

$$R = \det M - k(\text{trace} M)^2 \quad (3.28)$$

$$\det M = \lambda_1 \lambda_2 \quad \text{trace} M = \lambda_1 + \lambda_2 \quad k \in [0, 0.04] \quad (3.29)$$

It has been shown that Harris Method yields a precision only a few pixels in the positioning. To get sub-pixel accuracy position, the improved Sub-Pixel Accuracy Harris Corner Detector is introduced.

## B. Sub-Pixel Accuracy Harris Corner Detector

In order to concentrate on the area where they might be feature points, we first applied Harris Corner Detector at pixel level, and then we interpolated image gray values in the areas near detected corners. A 2D Gaussian filter was chosen for the interpolation:

$$g(x, y) = \frac{1}{k_1} e^{-\frac{(x-x_0)^2 + (y-y_0)^2}{2\delta^2}} \quad (3.30)$$

where  $(x_0, y_0)$  is the center of the filter.

After the interpolation, the corners were detected again at these interpolated areas. This procedure is called Sub-Pixel Accuracy Harris Corner Detection, and the corner position up to the sub-pixel accuracy can be detected.

## 3.6 Experiments

### 3.6.1 Synthetic Experiments

To test the sensitivity of our Biplanar Disparity Matrix measurement we first use some synthetic data experiment to do the work. Here the parameters used about the settings of the two cameras and the intrinsic parameters of the cameras as well as the alignment of the bumps on the wafer are quite alike those in the real image data experiment.

Firstly, we make the height of the bumps varies from 65 micron to 160 micron, with interval 5 micron, while keeping the other parameters constant, and try to find the relationship between the norm of  $\mathbf{D}$  and the height of bump. Since no outlier is involved here, we simply use DLT algorithm for homography estimation. Without any error or uncertainty considered, i.e., in the most ideal

case, norm of the Biplanar Disparity Matrix **D** has the following behavior as Fig. 3.9:

**Table 3.1: The parameters in synthetic experiments**

Parameters of the synthetic system	
Bump diameter	120 micron
Bump-bump distance	70 micron
Numbers of bumps per-inspection	20
Distance from wafer to camera frame	91mm
Angle between light source	15(degree)
Resolution of CCD	Du and Dv: 7.4micron

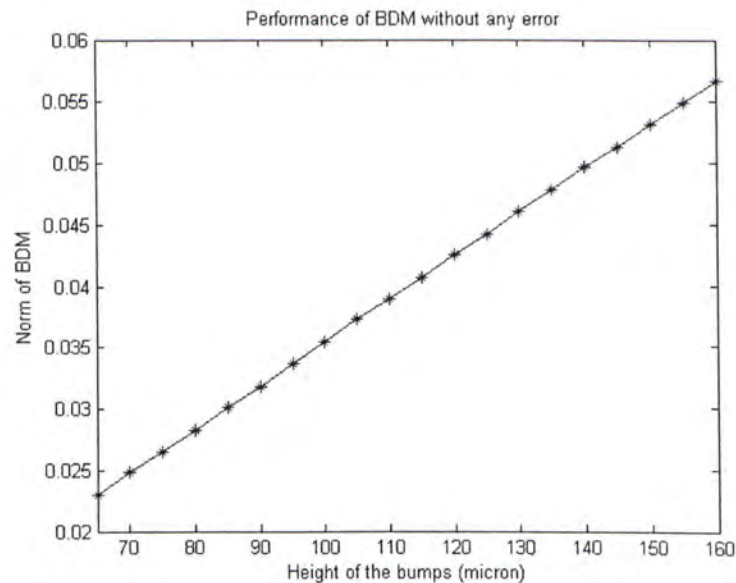


**Figure 3.9: Norm of BDM in the absence of any error or uncertainty.**

While, in the real world inspection process, there are most likely some errors exist. So we introduce three kinds of errors here, in order to make the experiment result much close to the real image data experiment. These uncertainties are as follows:

- 1) Quantization Error: Image is of limited resolution, thus image projection will be truncated to the position of the nearest pixel in the image.
- 2) Wafer Global Transformation: Ideally, the disparity matrix should be invariant with rigid transformation of the wafer. To ease our experiments, we consider the global transformation in two groups:
  - Wafer-plane transformation: there is only translation and rotation on the wafer plane. These are assumed to be 0 to 500 microns in translation, and 0 to 2 degree in rotation.
  - Wafer-tilting Transformation: there could be tilting of the wafer about its own plane due to the non-standard glue between the wafer and the feed-in system, which is about 5 degree in maximal.
- 3) Brightest Point Determination Uncertainty: Under our illumination system the peaks of the bumps would appear as brightest points in the image. However, due to image sensing saturation (the light reflected by the object has intensity so high that it goes beyond the sensing range of the CCD, and the object will display in the image as a white area where all the pixels are with the maximal intensity value), feature extraction, or



other factors, there could be uncertainty in determining the position of such brightest points in the image. We assume such uncertainty to be in the range  $\pm 1$  pixel.

Above uncertainties were added one by one to see their influences on the output, and the sensitivity analysis of D measurement is shown in the images below:

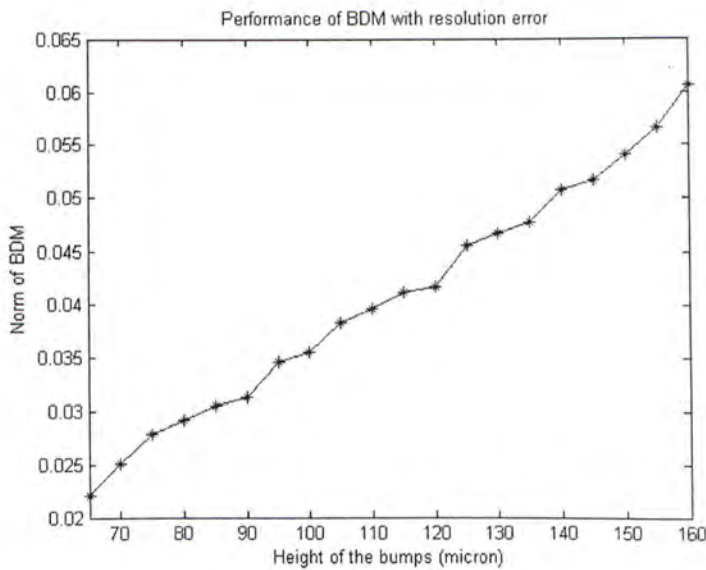


**Figure 3.10: Performance of BDM with resolution error**

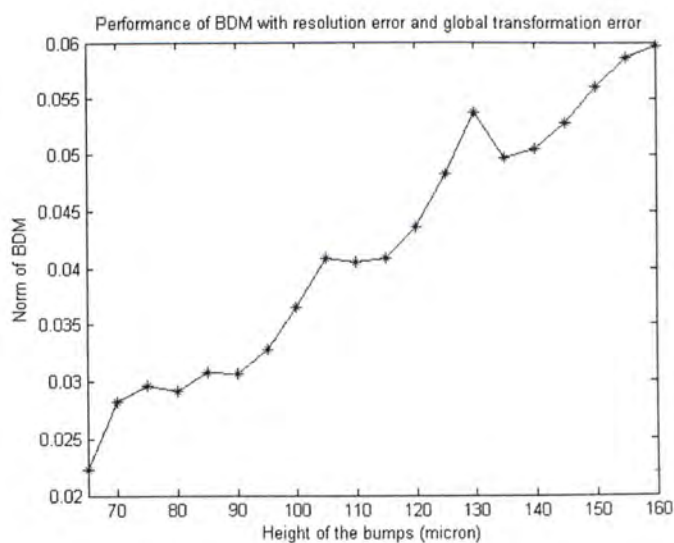


**Figure 3.11: Performance of BDM with resolution error and global transformation error**

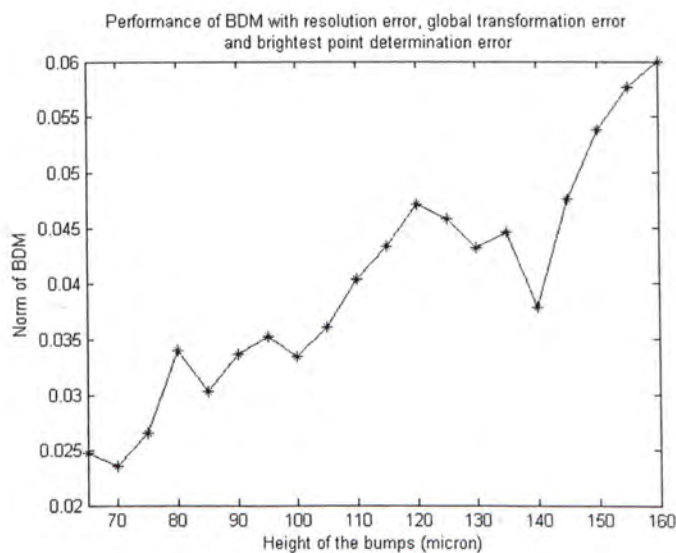


**Figure 3.12: Performance of BDM with resolution error, global transformation error and brightest point determination error**

Above results show that the norm of  $\mathbf{D}$  is proportional to the bump height in general, in spite of the limited errors exist in real situation, and the brightest points determination uncertainty is the main error source compared to the other disturbance.

### **3.6.2 Real image experiment**

In the real image data experiment, we use three different wafers with different size of bumps to test the validity of our method in real situation. The pictures were taken by sentec-405 CCD camera (752\*582) and Navitar Zoom 6000 lens, and the platform is shown in Fig. 3.13-15. The camera calibration is carried out using the camera calibration toolbox by Klaus Strobl and Wolfgang Sepp [43]. We take 7 pictures for each wafer, and a random but limited translation, rotation or tilting was given to the wafer when different pictures were taken, to simulate spatial disturbance in real world inspection. And the ranges of the errors are just as assumed in synthetic part. The wafer was put on a platform whose degree of freedom is five, to allow such a random disturbance.

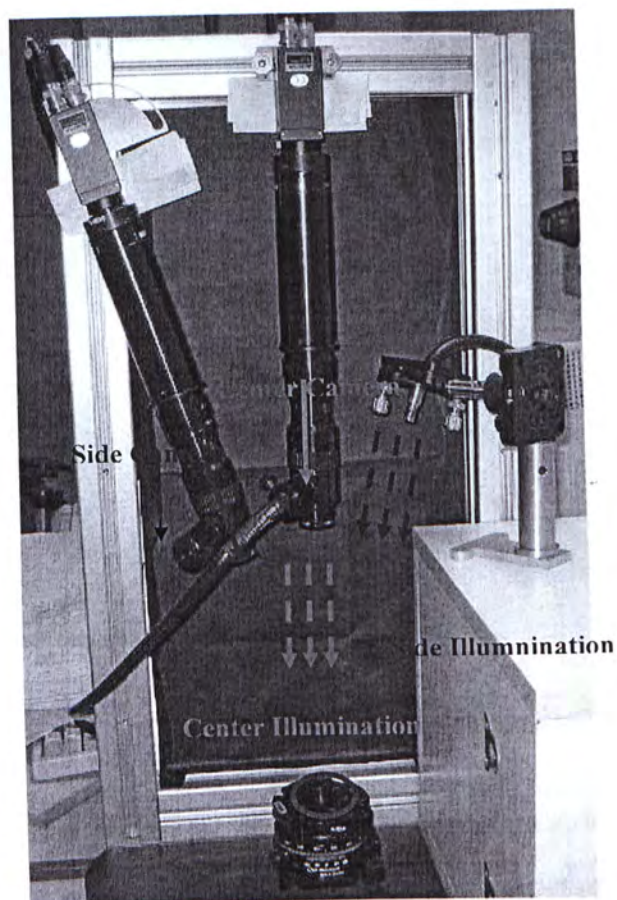


Figure 3.13: The imaging system

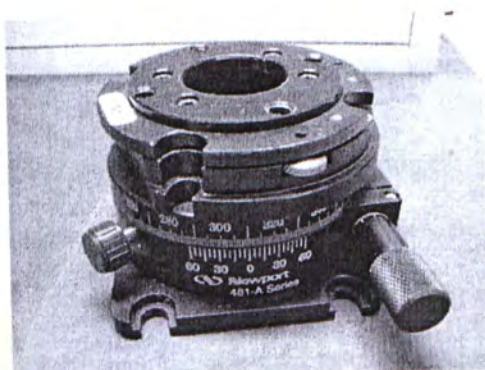
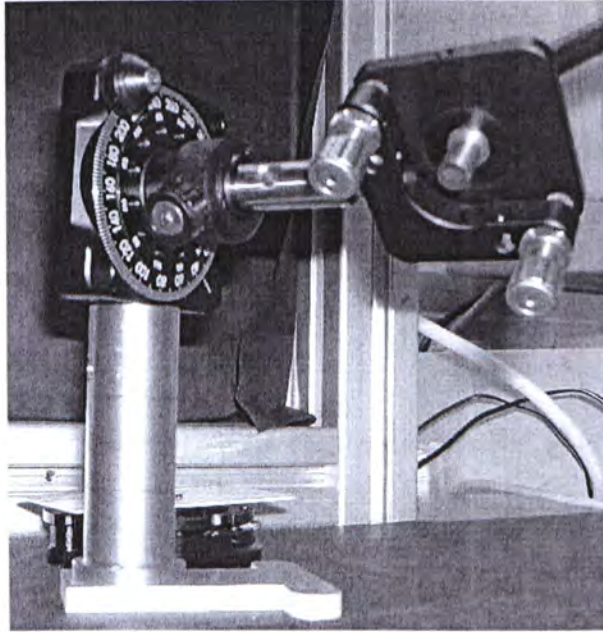


Figure 3.14: The 5 DoF platform for the wafer



**Figure 3.15: The parallel light source for the side camera**

In the image processing process we use RANSAC, a robust estimation method which constructs solutions from the minimum subset of data necessary [44]. The correspondences on the substrate are found by Harris Corner Detection, because it provides good repeatability under varying rotation and illumination.

### **Major steps**

**1) Imaging Setup:** Position the red parallel light source and the center camera in a head-on fashion to the wafer. Position the side camera at about 30deg separation from the center camera with respect to the wafer. Calibrate the Fundamental matrix  $F$  between the displaced cameras (a standard problem) [45] [46]. Position the blue light source on the opposite side of the side camera, as



illustrated in Fig. 3.4, until the blue spots observable by the side camera coincide, in 3D, with the red spots observable by the center camera. The whole thing is about positioning the blue light source such that (Blue light source, the side camera) and (Red light source, the center camera) have the same angle bisector orientation with respect to the wafer. This calibration only needs to be done one time.

**2) D Acquisition:** Get image point correspondences  $\{(\mathbf{x}_i', \mathbf{x}_i''), i = 1, 2, \dots\}$  over the bump peaks, and  $\{(\mathbf{x}_j^b, \mathbf{x}_j'^b), j = 1, 2, \dots\}$  over the bump bottoms. Estimate the homographies  $\mathbf{H}_l$  and  $\mathbf{H}_b$  using Equations (3.1) and (3.2), from the two sets of point correspondences. Use Equation (3.9) to measure  $\frac{\omega_l}{\alpha}$  and  $\frac{\omega_b}{\alpha}$  for  $\mathbf{H}_l$  and  $\mathbf{H}_b$  respectively. Use Equation (3.13) to come up with a measure of  $\mathbf{D}$  for the incoming wafer.

**3) Repeatability:** Give a random disturbance to the wafer position (translation, rotation, tilting), then take pictures by two cameras and repeat the above process of  $\mathbf{D}$  acquisition.

## Results

We take two wafers for comparison, marked as wafer A and wafer B. The bumps on wafer A are bigger than the ones on wafer B. During the real inspection, what we need is to check if the specimen wafer is good or bad, that is, to compare the specimen to the standard ones without getting the absolute

value of the bump height. So here we design some experiments to check the consistency of the algorithm. Each wafer was taken 21 pairs of pictures, divided into 3 subgroups, named as subgroup 1, 2, 3 with every subgroup owning 7 pairs of pictures. Within subgroup 1, random but limited tilting as described in previous part was added to the wafer. Similarly, pure translation and rotation as stated were added to subgroup 2 and 3. The sampled images are shown in Fig.3.16-21.

Every subgroup contains 7 pairs of pictures with different disturbance. Every pair of pictures are processed independently and induced a Biplanar Disparity Matrix  $\mathbf{D}$  for them, the result of the norm of  $\mathbf{D}$  are calculated and listed below in table 3.2-3.3, and the geometric expression of the result in two groups of curves are sketched in Fig.3.22.

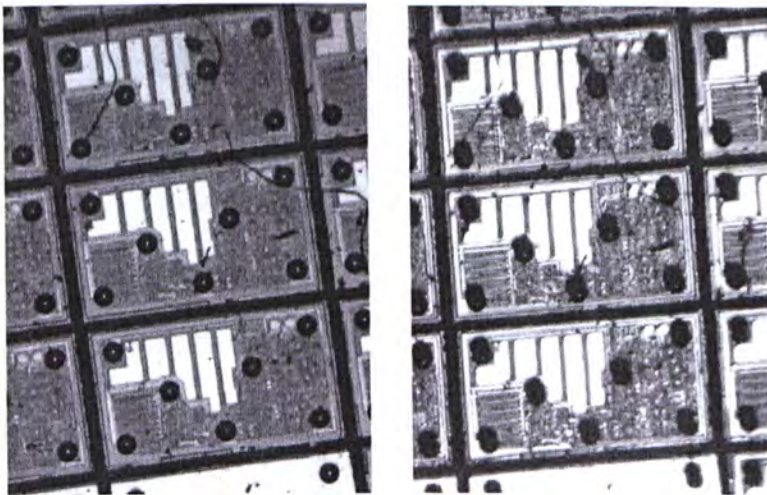


**Figure 3.16: A pair of pictures of wafer A in subgroup 1.**

**Left: the center image. Right: the side image**

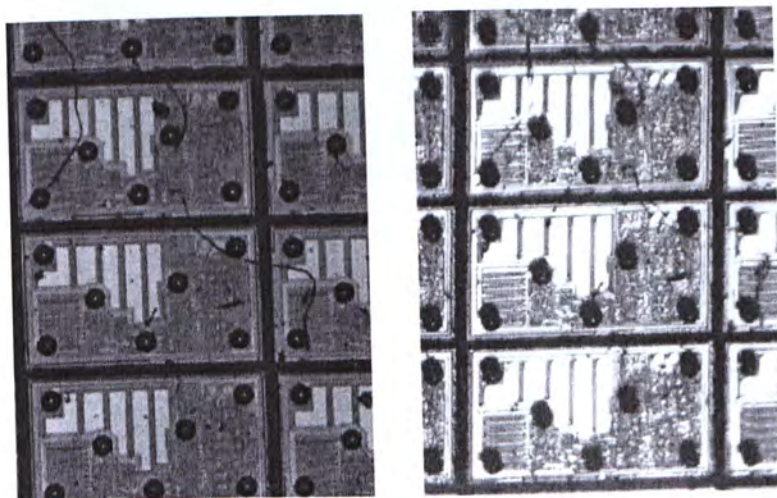


Figure 3.17: A pair of pictures of wafer A in subgroup 2.

Left: the center image. Right: the side image

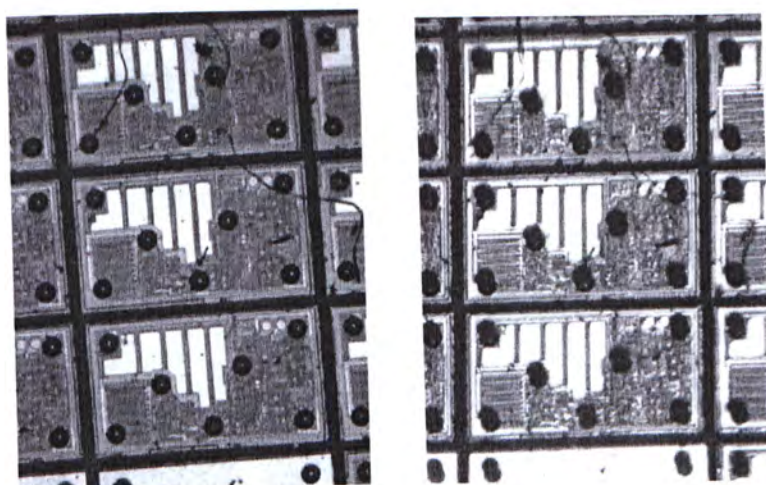


Figure 3.18: A pair of pictures of wafer A in subgroup 3.

Left: the center image. Right: the side image



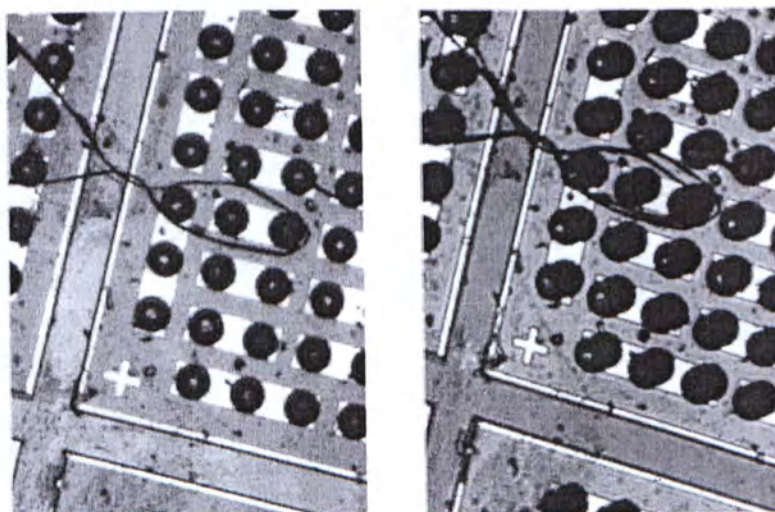


Figure 3.19: A pair of pictures of wafer B in subgroup 1.

Left: the center image. Right: the side image

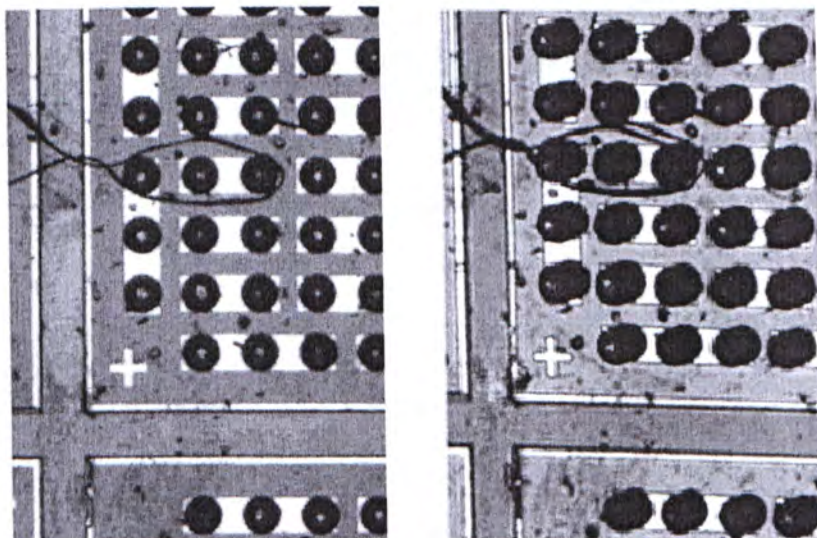


Figure 3.20: A pair of pictures of wafer B in subgroup 2.

Left: the center image. Right: the side image

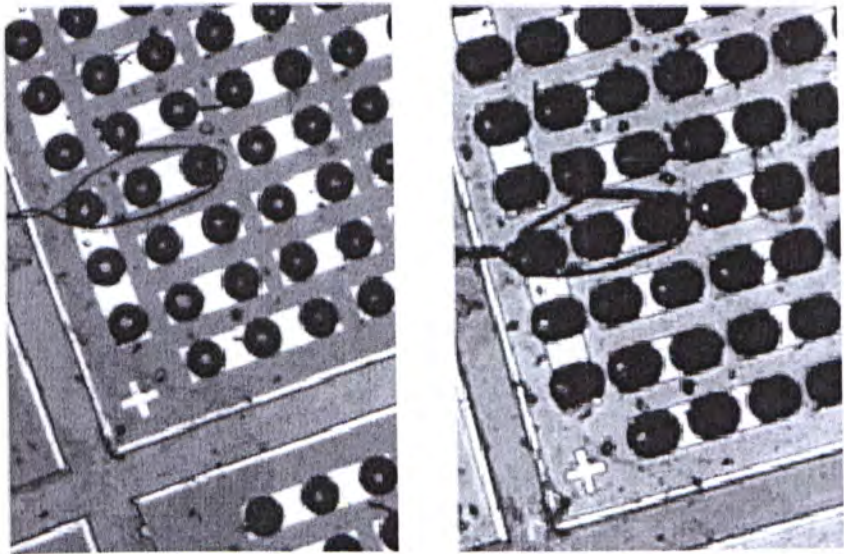


Figure 3.21: A pair of pictures of wafer B in subgroup 3.

Left: the center image. Right: the side image

Table 3.2: Norm of BDM by wafer A

Pic. No.	1	2	3	4	5	6	7	Mean	Fluc.
Sub group1	0.0302	0.0253	0.0243	0.0240	0.0300	0.0280	0.0266	0.0269	9.54%
Sub group2	0.0252	0.0272	0.0271	0.0275	0.0268	0.0256	0.0261	0.0265	3.30%
Sub group3	0.0254	0.0263	0.0259	0.0273	0.0262	0.0264	0.0269	0.0263	2.37%

Table 3.3: Norm of BDM by wafer B

Pic. No.	1	2	3	4	5	6	7	Mean	Fluc.
Sub group1	0.0121	0.0104	0.0131	0.0119	0.0104	0.0108	0.0126	0.0116	9.37%
Sub group2	0.0104	0.0118	0.0108	0.0115	0.0108	0.0107	0.0104	0.0109	4.92%
Sub group3	0.0114	0.0103	0.0109	0.0113	0.0110	0.0114	0.0106	0.0110	3.84%



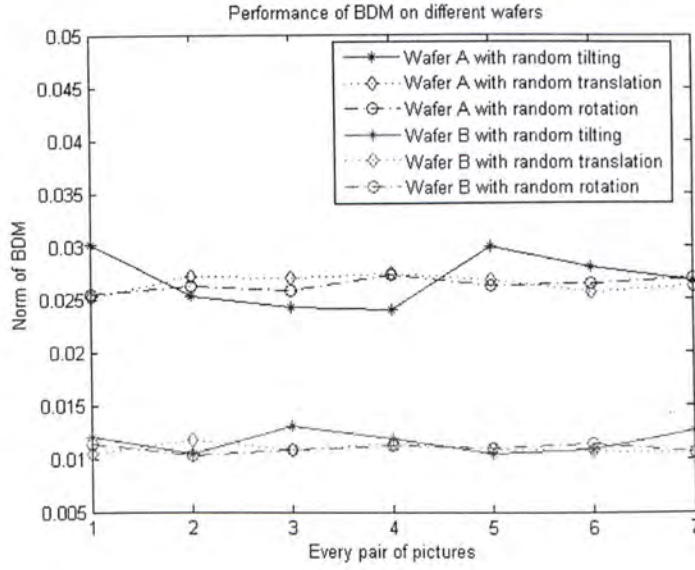


**Figure 3.22: Norm of  $D$  induced by two different wafers with variant disturbance added**

The experiment results show that the variant disturbance did cause fluctuation of the norm of  $D$ . Among the three kinds of disturbance, tilting has the most influence on the result, since it will cause the deviation of the brightest points to the position of top points. The absolute value of the fluctuation of wafer A is bigger than that of wafer B. This is because the bumps on wafer A is bigger and so the top area is flatter than those on wafer B, which will cause greater uncertainty in brightest point determination. In spite of the fluctuation, the two groups of  $D$  norm are well separated according to the different size of the bumps. This proves the effectiveness of the Biplanar Disparity Method.

### 3.7 Conclusion and problems

By now we propose a bump height inspection method based on homography, named as Biplanar Disparity Method. From the above experimental results, both the synthetic experiment and the real data experiment show that the Biplanar Disparity Matrix is sensitive enough to the change in bump height, even under a number of errors and uncertainties. These results can preliminary testify that the Biplanar Disparity matrix  $\mathbf{D}$ , which includes the planar information of both of the top plane and the substrate plane of the bumps, has a tight relationship with the relative position of these two planes.

But both the synthetic and real data experiments have indicated that the algorithm is quite sensitive to the brightest points determination uncertainties. In the synthetic results, the synthetic brightest point determination uncertainties causes bigger fluctuation to the norm of  $\mathbf{D}$ , and in real data results, the wafer with bigger bump also has bigger fluctuation according to Table 3.2 and 3.2, due to the flatter top area on the bump. This is understandable for the parameter we choose, the planar homography, is sensitive to the correspondences error. So in the following part, we will focus on this problem to make some revision to the BDM.

## Chapter 4

### PARAPLANAR DISPARITY METHOD

In previous part we proposed a method to massively inspect the bump height without explicit 3D reconstruction, which converts the height inspection problem to a question about the distance between two planes, by a system setting pictured as Fig. 3.4. It explores two certain planes, as explained in Fig. 3.3. One contains the top points of most of the bumps and the other contains the substrate. First to find out the homography matrices of these two planes by robust estimation. In this process, the outliers, which refers to the bumps too tall or too short, if exists, will be detected. If no defect was found at this stage, the so called Biplanar Disparity Matrix  $\mathbf{D}$  will be calculated by the two homography matrices and the fundamental matrix of the camera system. By analyzing this matrix  $\mathbf{D}$  we could get the information of the distance between these two planes, and thus the information of the bump heights.

This Biplanar Disparity Method takes the top and the substrate planes as the processing subject and deals with the global parameter, the homography matrix, thus could check massive bumps at one time. But one problem is that the homography matrix is quite sensitive to noise [47]. This may cause poor tolerance of noise or error in feature detection and matching. In this paper, we will improve this method by bring in the parallel constraint according to the real

situation in industry. An algorithm based on the Biplanar Disparity Method, but specially designed to deal with two parallel planes to achieve more robust and accurate output, will be illustrated here.

## 4.1 The Parallel Constraint

In bump height inspection, the defect is presented as two cases:

- 1) The defect marked as non-coplanarity, means some of the bumps on the wafer are too tall or too short, nevertheless most of the bumps are considered as golden ones, as shown in Fig. 4.1a.
- 2) The BGA is globally too high or too short. It means that all of the bumps on the wafer are of the same but wrong height, as shown in Fig. 4.1b.

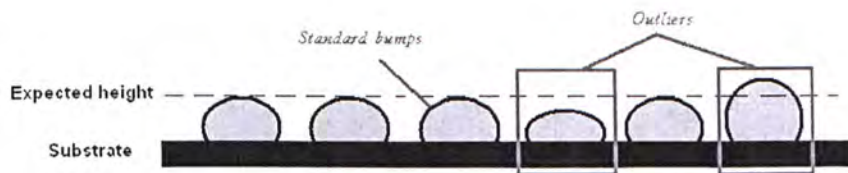


**Figure 4.1a: Some of the bumps are too tall or too short**



**Figure 4.1b: The bumps are globally too short (or too tall)**

**Figure 4.1: The presentation of 3D defects**

In both of these two cases, the majority of the bumps are of the same height. When we estimate the top plane, the minority bumps which are too tall or too short, considered as outliers, will be picked out by robust estimation, and the top plane we got will consist of points that have the same distance to the substrate. We observe that as the visual field of the inspected die is very small relative to the imaging distance, the bump and substrate planes can well be regarded as parallel for the limited segments of theirs that cover the inspected die. In other words, we could reformulate the homography estimation problem as one of estimating two homographies that are induced by parallel planes in 3D. With this, the feature points for estimating  $\mathbf{H}_t$  and  $\mathbf{H}_b$  separately could be combined together as a single set for the simultaneous estimation of the two homographies, thereby increasing the effective number of data points for the estimation of either. Below we show how we can do that.

Denote the homography matrix of  $\Pi_t$  and  $\Pi_b$  as  $\mathbf{H}_t$  and  $\mathbf{H}_b$  respectively, then

$$\mathbf{H}_t \cong \mathbf{A}'\mathbf{R}^{-1}(\mathbf{I} - \mathbf{t} \frac{\hat{\mathbf{n}}_t^T}{d_t})\mathbf{A}^{-1} \quad (4.1)$$

$$\mathbf{H}_b \cong \mathbf{A}'\mathbf{R}^{-1}(\mathbf{I} - \mathbf{t} \frac{\hat{\mathbf{n}}_b^T}{d_b})\mathbf{A}^{-1} \quad (4.2)$$



Here  $\mathbf{A}$ ,  $\mathbf{A}'$ ,  $\mathbf{R}$  and  $t$  are intrinsic and extrinsic camera parameters of the imaging system in Fig. 3.4,  $\mathbf{I}$  is the identity matrix,  $\hat{\mathbf{n}}_l$  and  $\hat{\mathbf{n}}_b$  are the unit surface normal of the planes,  $d_l$  and  $d_b$  are the distance from the camera center to the planes.

If  $\Pi_l$  and  $\Pi_b$  are parallel, we have  $\hat{\mathbf{n}}_l = \hat{\mathbf{n}}_b = \hat{\mathbf{n}}$ ,  $d_l = d_b + \bar{d}$ , where  $\bar{d}$  is the signed evaluation difference between the two planes, which reveals the bump height information. Substitute the parallel relations into (4.1) and (4.2), we get

$$\mathbf{H}_l \cong \mathbf{A}'\mathbf{R}^{-1}(\mathbf{I} - t\frac{\hat{\mathbf{n}}^T}{d_b + \bar{d}})\mathbf{A}^{-1} \quad (4.3)$$

$$\mathbf{H}_b \cong \mathbf{A}'\mathbf{R}^{-1}(\mathbf{I} - t\frac{\hat{\mathbf{n}}^T}{d_b})\mathbf{A}^{-1} \quad (4.4)$$

Since in practical imaging setting  $\bar{d} \ll d_b$ , we have  $\frac{1}{d + \bar{d}} \approx \frac{1}{d}(1 - \frac{\bar{d}}{d})$ , and the following approximation:

$$\begin{aligned} \mathbf{H}_l &\cong \mathbf{A}'\mathbf{R}^{-1}(\mathbf{I} - t\frac{\hat{\mathbf{n}}^T}{d_b + \bar{d}})\mathbf{A}^{-1} \\ &\cong \eta\mathbf{H}_b + \frac{\bar{d}}{d_b}\mathbf{A}'\mathbf{R}^{-1}\mathbf{A}^{-1} - \eta\frac{\bar{d}}{d_b}\mathbf{H}_b \\ &\cong \eta(1 - \frac{\bar{d}}{d_b})\mathbf{H}_b + \frac{\bar{d}}{d_b}\mathbf{A}'\mathbf{R}^{-1}\mathbf{A}^{-1} \end{aligned} \quad (4.5)$$

for some scaling parameter  $\eta$ .

Equation (4.5) could be expressed as:

$$\mathbf{H}_t \cong \mathbf{H}_b + \frac{\eta' \frac{\bar{d}}{d_b}}{(1 - \frac{\bar{d}}{d_b})} \mathbf{A}' \mathbf{R}^{-1} \mathbf{A}^{-1} \cong \mathbf{H}_b + \lambda \mathbf{A}' \mathbf{R}^{-1} \mathbf{A}^{-1} \quad (4.6)$$

Here  $\lambda$  is a scaling factor relating to the camera parameters, the imaging distance, the bump height and the actual homography matrix of the substrate plane we get (because the homography matrix is up to a scale, what we actually use in calculation is just one of the family, usually the one by some kind of normalization). But we do NOT need the exact value of  $\lambda$ , what we obtain here is the relation between the two homography matrices induced by two parallel and very close to each other planes. With this relationship, we could integrate the correspondences from  $\Pi_t$  and the ones from  $\Pi_b$  into a group for homography estimation, to achieve more accurate and robust output as well as a more clean calculation.

## 4.2 Homography estimation

The DLT (Direct Linear Transformation) algorithm utilizes the point correspondences for homography estimation, without requiring the epipolar geometry as a precondition or using other high order curves, and could avoid compounding of the uncertainty in the estimation of these primary structures before computing the homography. And it could be easily implemented by SVD analysis. So we take the DLT as kernel algorithm for coarse to fine homography estimation.

Denote  $\mathbf{M} = \mathbf{A}'\mathbf{R}^{-1}\mathbf{A}^{-1}$ , then

$$\mathbf{H}_t \cong \mathbf{H}_b + \lambda \mathbf{M} \quad (4.7)$$

$$\mathbf{H}_t \cdot \mathbf{x}_t \cong (\mathbf{H}_b + \lambda \mathbf{M}) \cdot \mathbf{x}_t \cong \mathbf{x}_t' \quad (4.8)$$

$$\mathbf{H}_b \cdot \mathbf{x}_b \cong \mathbf{x}_b' \quad (4.9)$$

Here  $\mathbf{x} = (x_1, x_2, x_3)^T$  is the homogeneous coordinates of the image points.

Utilize equation (4.8) and (4.9), the image point correspondences  $(\mathbf{x}_t, \mathbf{x}_t')$  from  $\Pi_t$  and the image point correspondences  $(\mathbf{x}_b, \mathbf{x}_b')$  from  $\Pi_b$  are allowed to be combined forming a new big group to compute  $\mathbf{H}_b$ , as well as  $\mathbf{H}_t$ . For every pair of correspondences from the substrate plane  $(\mathbf{x}_b, \mathbf{x}_b')$ :

$$\begin{bmatrix} \mathbf{0}^T & -x_{b3}' \mathbf{x}_b'^T & x_{b2}' \mathbf{x}_b'^T \\ x_{b3}' \mathbf{x}_b'^T & \mathbf{0}^T & -x_{b1}' \mathbf{x}_b'^T \end{bmatrix} \begin{pmatrix} \mathbf{h}_1 \\ \mathbf{h}_2 \\ \mathbf{h}_3 \end{pmatrix} = \mathbf{0} \quad (4.10)$$

$\begin{matrix} & & & & & & & & \\ & & & & & & & & \\ & & & & & & & & \\ & & & & & & & & \\ & & & & & & & & \\ & & & & & & & & \\ & & & & & & & & \\ & & & & & & & & \\ & & & & & & & & \end{matrix}$ 
 $\begin{matrix} 2 \times 9 & & 9 \times 1 \end{matrix}$

For every pair of correspondences from the top plane  $(\mathbf{x}_t, \mathbf{x}_t')$ :

$$\begin{bmatrix} \mathbf{0}^T & -x_{t3}' \mathbf{x}_t'^T & x_{t2}' \mathbf{x}_t'^T \\ x_{t3}' \mathbf{x}_t'^T & \mathbf{0}^T & -x_{t1}' \mathbf{x}_t'^T \end{bmatrix} \begin{pmatrix} \mathbf{h}_1 + \lambda \mathbf{m}_1 \\ \mathbf{h}_2 + \lambda \mathbf{m}_2 \\ \mathbf{h}_3 + \lambda \mathbf{m}_3 \end{pmatrix} = \mathbf{0} \quad (4.11)$$

$\begin{matrix} & & & & & & & & \\ & & & & & & & & \\ & & & & & & & & \\ & & & & & & & & \\ & & & & & & & & \\ & & & & & & & & \\ & & & & & & & & \\ & & & & & & & & \\ & & & & & & & & \end{matrix}$ 
 $\begin{matrix} 2 \times 9 & & 9 \times 1 \end{matrix}$

That is

$$\begin{bmatrix} \mathbf{0}^T & -x_{t3}' \mathbf{x}_t'^T & x_{t2}' \mathbf{x}_t'^T \\ x_{t3}' \mathbf{x}_t'^T & \mathbf{0}^T & -x_{t1}' \mathbf{x}_t'^T \end{bmatrix} \begin{pmatrix} \mathbf{h}_1 \\ \mathbf{h}_2 \\ \mathbf{h}_3 \end{pmatrix} + \lambda \begin{bmatrix} \mathbf{0}^T & -x_{t3}' \mathbf{x}_t'^T & x_{t2}' \mathbf{x}_t'^T \\ x_{t3}' \mathbf{x}_t'^T & \mathbf{0}^T & -x_{t1}' \mathbf{x}_t'^T \end{bmatrix} \begin{pmatrix} \mathbf{m}_1 \\ \mathbf{m}_2 \\ \mathbf{m}_3 \end{pmatrix} = \mathbf{0} \quad (4.12)$$

$\begin{matrix} & & & & & & & & \\ & & & & & & & & \\ & & & & & & & & \\ & & & & & & & & \\ & & & & & & & & \\ & & & & & & & & \\ & & & & & & & & \\ & & & & & & & & \\ & & & & & & & & \end{matrix}$ 
 $\begin{matrix} 2 \times 9 & & 9 \times 1 \end{matrix}$

Combine equation (4.10) and (4.12) together:

$$\begin{bmatrix} \mathbf{0}^T & -x_3' \mathbf{x}^T & x_2' \mathbf{x}^T \\ x_3' \mathbf{x}^T & \mathbf{0}^T & -x_1' \mathbf{x}^T \end{bmatrix}_{2 \times 10} \begin{bmatrix} p_1 \\ p_2 \end{bmatrix} \begin{pmatrix} \mathbf{h}_1 \\ \mathbf{h}_2 \\ \mathbf{h}_3 \\ \lambda \end{pmatrix}_{10 \times 1} = \mathbf{0} \quad (4.13)$$

Equation (4.13) will be used as a uniform one for correspondences from both the top and the substrate to estimate  $\mathbf{H}_b$ . Here  $\mathbf{h}_i^T$  and  $\mathbf{m}_j^T$  ( $i, j = 1, 2, 3$ ) denote the row vector of the matrices  $\mathbf{H}_b$  and  $\mathbf{M}$ . And

$$p_i = \begin{cases} \begin{bmatrix} 0^T & -x_3' \mathbf{x}^T & x_2' \mathbf{x}^T \end{bmatrix} \begin{pmatrix} \mathbf{m}_1 \\ \mathbf{m}_2 \\ \mathbf{m}_3 \end{pmatrix} & \text{for } (\mathbf{x}_b, \mathbf{x}_b') \\ 0 & \text{for } (\mathbf{x}_t, \mathbf{x}_t') \end{cases} \quad (4.14)$$

$$p_2 = \begin{cases} \begin{bmatrix} x_3' & \mathbf{x}^T & \mathbf{0}^T & -x_1' & \mathbf{x}^T \end{bmatrix} \begin{pmatrix} \mathbf{m}_1 \\ \mathbf{m}_2 \\ \mathbf{m}_3 \end{pmatrix} & \text{for } (\mathbf{x}_b, \mathbf{x}_b') \\ 0 & \text{for } (\mathbf{x}_t, \mathbf{x}_t') \end{cases} \quad (4.15)$$

The Biplanar Disparity Method estimates  $\mathbf{H}_t$  and  $\mathbf{H}_b$  from the image point correspondences over  $\Pi_t$  and  $\Pi_b$  respectively. Due to the inaccuracy and error in feature extraction and image matching, the resulted homography matrices may deviate the actual value induced by the two planes we concerned, and most of the time, are corresponding to some two non-parallel close to  $\Pi_t$  and  $\Pi_b$ . But Para-planar Disparity Method takes this parallel constraint into account, and

as a result the non-parallel error is avoided. At the mean while, as we combine the two set of correspondences together into a big group, the size of the sample set for homography matrix estimation has been expanded to approximate double, which makes the algorithm more robust to the perturbation from the feature detection and matching phase.

### **4.3. Experiment:**

#### **4.3.1 Synthetic Experiment:**

Firstly we do some synthetic experiments to see how much the performance of the Para-planar Disparity Method is improved at the homography estimation stage, since this is the part the new method directly acts on and also the disparity matrix is based on. Here Monte Carlo simulation was made to visually compare the variance of the result [48].

Here the parameters used about the settings of the two cameras and the intrinsic parameters of the cameras as well as the alignment of the bumps on the wafer are quite alike those in the real image data experiment.

Setting as stated in Table 4.1, we get 20 pairs of image point correspondences on the top plane denoted as  $(x_t, x_t')$ , and 20 pairs of the image point



correspondences on the substrate plane denoted as  $(x_b, x_b')$ . One pixel Gaussian noise was added to the correspondences and the noisy data was used for homography estimation. A certain point on the centre image is projected by the  $H_{t1}$  and  $H_{t2}$ , from Biplanar method and Paraplanar method respectively, to the side image. 100 trials were made, and monte carlo simulation is adopted here. The noise free output should be a point at (16, 5) on the side image, but due to the Gaussian noise added, the actual output is a family of points around (16, 5). From Fig. 4.2b-4.2c, we find the points family induced by Paraplanar method is less sparse than biplanar one, reveals the paraplanar method is more robust to the perturbation of error in matching at homography stage.

**Table 4.1: The parameters in synthetic experiments**

Parameters of the synthetic system	
Bump diameter	120 micron
Bump-bump distance	70 micron
Numbers of bumps per-inspection	20
Distance from wafer to camera frame	91mm
Angle between light source	15(degree)
Resolution of CCD	Du and Dv: 7.4micron

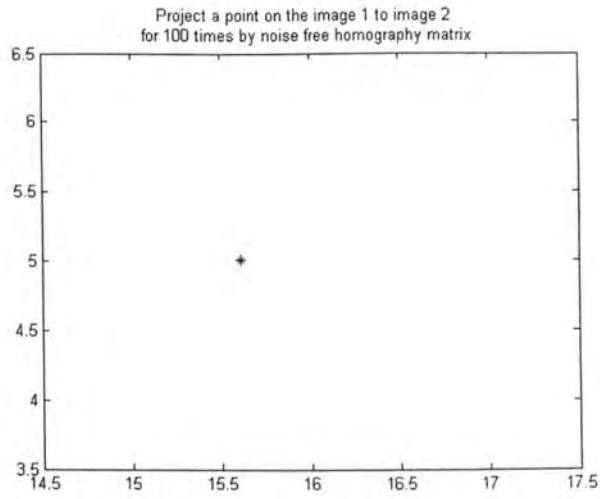


**Figure 4.2a: The ideal projection of a certain point on the center image  
to the side image should be a single point.**

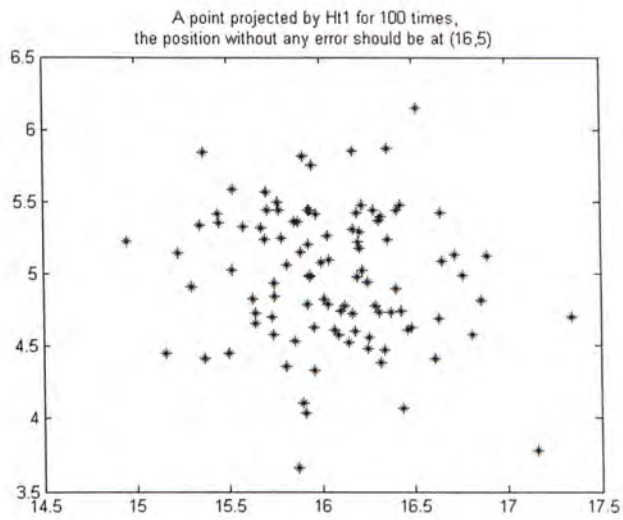


**Figure 4.2b: The projection image of a certain point by the noisy  
homography calculated by BDM**

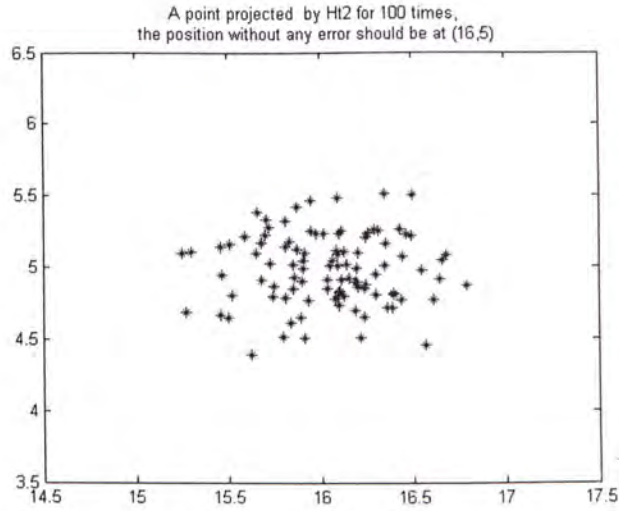


**Figure 4.2c: The projection image of a certain point by the noisy homography calculated by PDM**

**Figure 4.2: The comparison of the robustness of homography estimation of BDM and PDM.**

Then we fix the bump height at 60 microns, and add one pixel Gaussian noise to the image correspondences. These synthetic noisy data is used to estimate both the Biplanar Disparity Matrix and Paraplanar Disparity Matrix. The norm of BDM and PDM are then computed respectively as a reflection of the bump height. Ideally the figure will be a straight line, as shown in fig. 4.3a, but the Gaussian noise will result in fluctuation of the actual output. Fig. 4.5b and fig. 4.5c is the results of the two methods, show the improvement of robustness to the noise in image point correspondences.

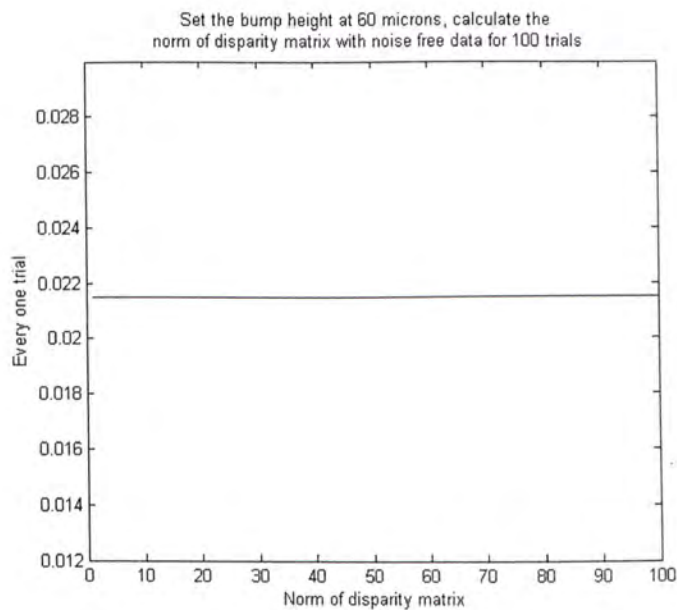


**Figure 4.3a: The noise free output of norm of  $D$  by fixed height bumps should be a straight line.**

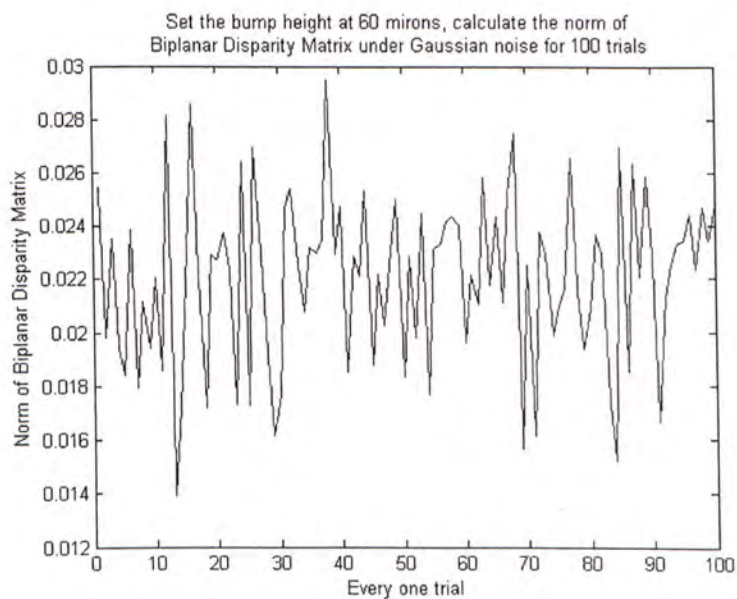


**Figure 4.3b: The output of BDM under Gaussian noise.**

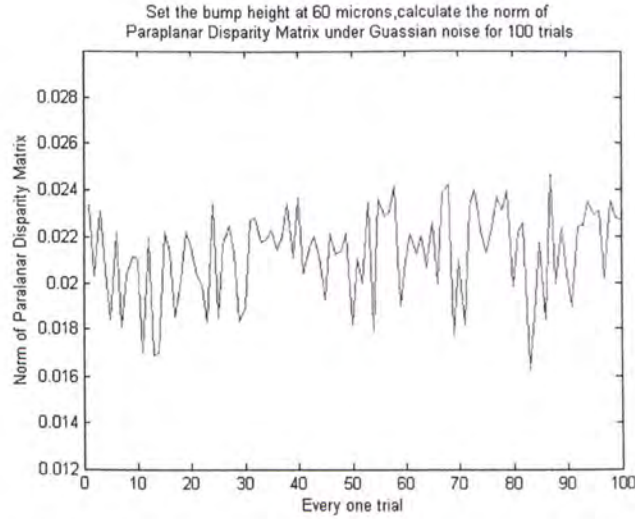


**Figure 4.3c: The output of PDM under Gaussian noise**

**Figure 4.3: The comparison of the robustness of the BDM and PDM on bump height inspection.**

### 4.3.2 Real Image Experiment:

The real image data is captured by the same imaging system as we introduced in chapter 3. We take 7 pairs of pictures of one wafer, and a random but limited translation along x or y or z axis (0 to 500 microns), rotation along z axis (0 to 2 degree), and tilting up to 2 degree was given to the wafer when different pictures were taken, to simulate spatial disturbance caused by feed in system in real industrial inspection. The wafer was put on a platform whose degree of freedom is five, to allow such a random disturbance. Pictures of the wafer are shown below in fig. 4.4-4.10, and the detailed steps are illustrated in chapter 3 for reference.



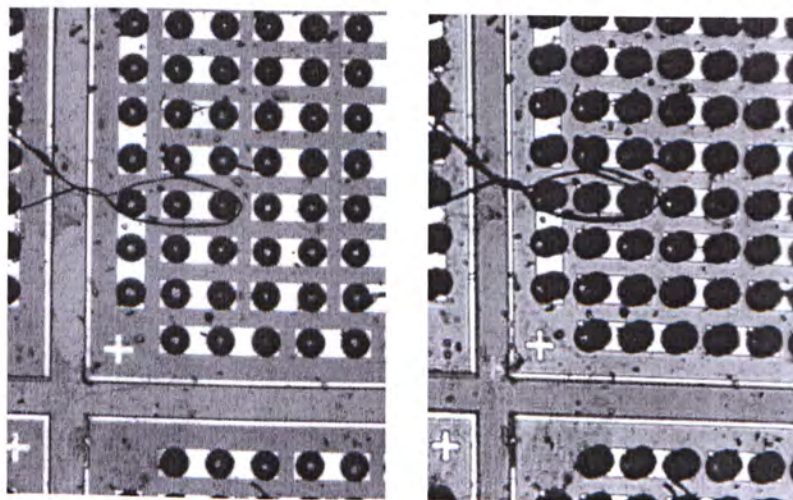


Figure 4.4: Real image for BDM and PDM – Picture pair 1

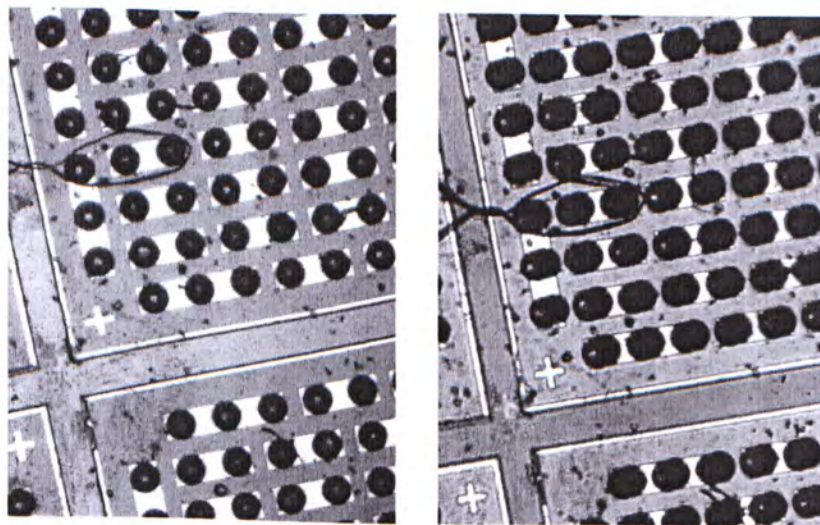


Figure 4.5: Real image for BDM and PDM – Picture pair 2

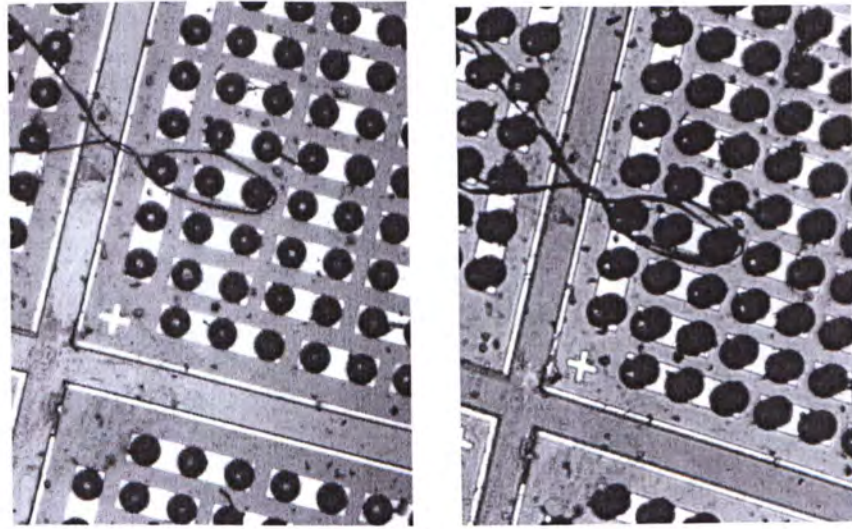


Figure 4.6: Real image for BDM and PDM – Picture pair 3

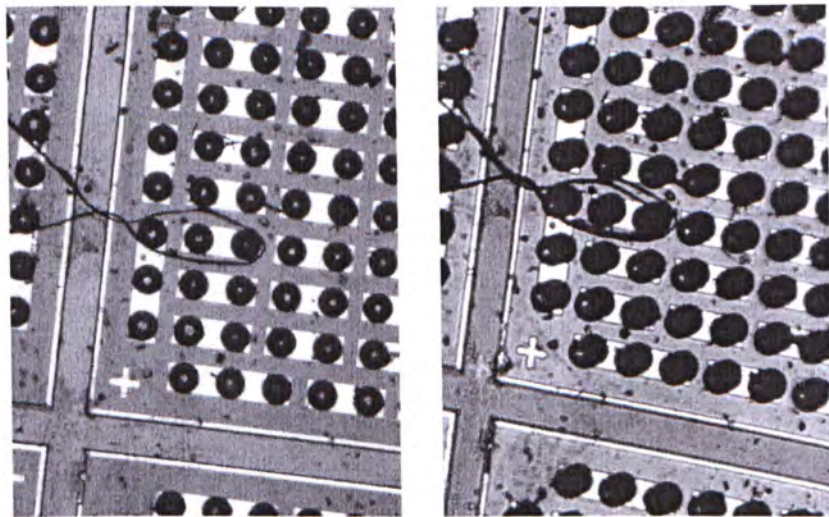


Figure 4.7: Real image for BDM and PDM – Picture pair 4



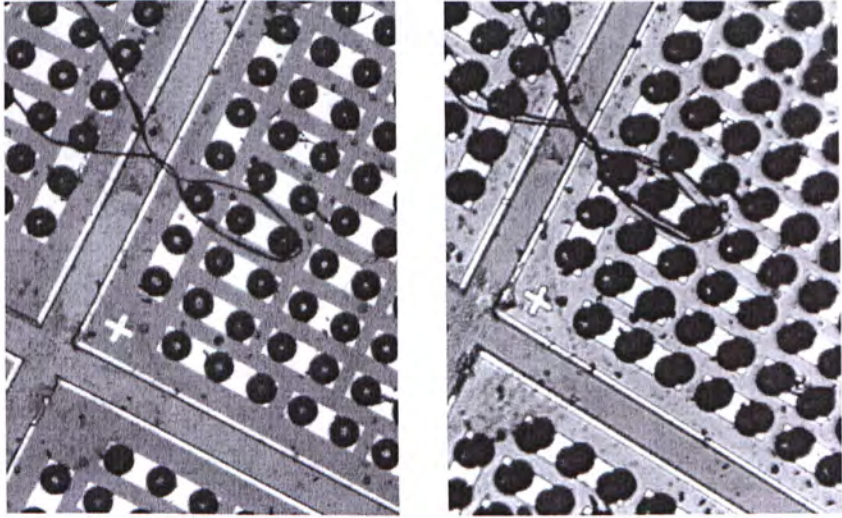


Figure 4.8: Real image for BDM and PDM – Picture pair 5

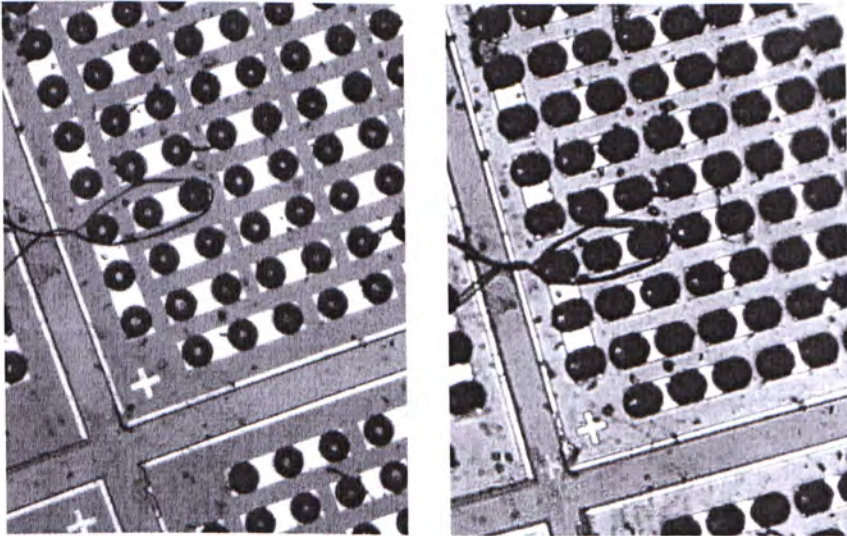
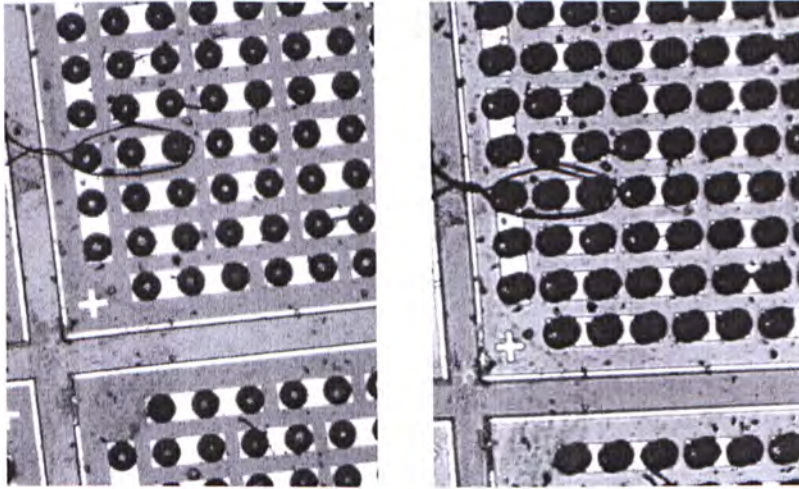


Figure 4.9: Real image for BDM and PDM – Picture pair 6



**Figure 4.10: Real image for BDM and PDM – Picture pair 7**

The norm of Paraplanar Disparity Matrix and Biplanar Disparity Matrix are estimated respectively from the same set of image data shown above. Every set of pictures (one set includes one center image and one corresponding side image) will induce one value of norm disparity matrix, and totally 7 value will be obtained by each method. Ideally the 7 value will be identical and the figure will be a straight line. But due to the global disturbance (rotation and translation stated above), fluctuation is observed. Table 4.2 tells the result and the fluctuation of the result are calculated. The data is plotted in fig.4.11.

**Table 4.2: Comparison of the results of BDM and PDM**

Pic. No.	1	2	3	4	5	6	7	Mean	Fluc.
<b>BDM</b>	0.0121	0.0094	0.0122	0.0112	0.0126	0.0104	0.0097	<b>0.0111</b>	<b>11.48%</b>
<b>PDM</b>	0.0115	0.0102	0.0116	0.0111	0.0118	0.0107	0.0103	<b>0.0110</b>	<b>5.76%</b>

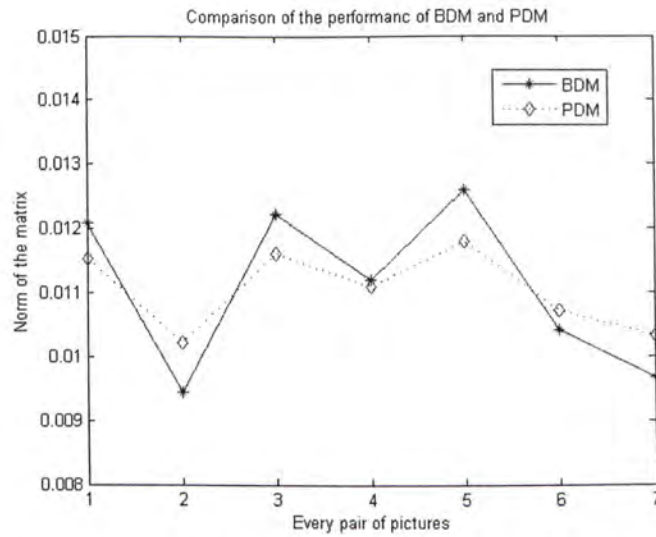


**Figure 4.11: Comparison of the performance of BDM and PDM**

The data table shows the mean value of BDM and PDM are almost the same, but the fluctuation by PDM has been reduced to half of that by BDM, which demonstrate the effectiveness of the PDM on the sensitivity to the bump height and the improvement on the robustness to the noise.

The curves plotted in Fig.4.11 makes above conclusion easier to see and it also exhibits the agreement between the two curves on the oscillating trend. This is obvious for the results are calculated by the same data set.



## Chapter 5

# CONCLUSION AND FUTURE WORK

### 5.1 Summary of the contributions

In this thesis we proposed a method for massively bump height inspection without explicit 3D reconstruction. It investigates the two planes encoding the bump height information, and creatively makes use of the mirror like reflectivity of the bump surface. In the improved version, also the parallel constraint of the two planes are explored and more robust and elegant output is gained. Both the synthetic experiment and the real data experiment show the Biplanar Disparity matrix and Parallel Disparity matrix has a tight relationship with the relative position of these two planes, and is sensitive enough to the change in bump height, even under a number of errors and uncertainties.

This idea solves the problem of finding correspondences on the textureless bump surface and the difficulty caused by the great difference in reflectivity between the bump surface and substrate. The use of the global parameter, the homography, makes the massive and parallel processing possible. The idea is based on thought of problem conversion, that is, from problem of height inspection to the problem of top points investigation, then to the problem of two planes investigation. It involves an extraction and reforming of the top points on

the bumps, and in this way to avoid the explicit 3D reconstruction. The whole effort is made for the improvement of the efficiency of the inspection.

An imaging system is designed to realize the algorithm. The system consists of two sets of CCD, lens and light sources. Once the system is set up and calibrated, no moving part is involved in the imaging system during the whole inspection process. This will greatly save the time and reduce the external uncertainty. Getting rid of the high requirement of the positioning accuracy in moving parts will also significantly reduce the potential cost.

## **5.2 Future Work**

Both the synthetic and real data experiments show that the result will be affected to a significant extent by the brightest point determination. This makes the task of fine locating and matching of the top points stringent, especially when malformation of the bumps or abrasion of the top area happens. In our real data experiment, we met the case of abrasion, and the brightest point we concerned has become a "brightest area". We deal with it by finding the center point of the brightest area. This works in most of the cases but the case that the abrasion deviates the top area. Future work should address here not only how to find the top point in ill conditioned case, but also how to alleviate the dependence of the result on the precision of the locating.

In our method we just investigate the norm of the disparity matrix. Both the bump height and the norm of the matrix is a scalar, so to study the relationship

between these two scalars is a straightforward thought, as our method does, and it does prove the effectiveness of this idea. But more information is ensealed in the nine entries of the disparity matrix. More discoveries are expected in further studying of the disparity matrix.

Finally, the whole inspection system needs to be integrated into a totally automatic one, including the feed in system, the camera calibration processing, the image grabbing system, and the inspection processing.

## Publication related to this work:

Dong Mei, Ronald Chung, "Height Inspection of Wafer Bumps without Explicit 3D Reconstruction" IS&T/ SPIE 18th Annual Symposium on Electrical Imaging at San Jose, USA. in January, 2006.

## BIBLIOGRAPHY

[1] Rao Tummala, "Fundamentals of Microsystems Packaging", *McGraw-Hill Professional, the first edition (May 8, 2001)*

[2] Steve Berry, "Reaching HDI comfort levels", *High-Density Interconnect, vol. 1, 1998, p14.*

[3] Jerry Murry, "Flip Chip Technology", *High-Density Interconnect, vol. 1, 1998, p40.*

[4] L. F. Miller, "Controlled Collapse Reflow Chip Joining," *IBM J. Res. & Dev. 13, 239-250 (May 1969).*

[5] P. A. Totta, "Flip-Chip Solder Terminals," *Proceedings of the 21st Electronics Components Conference, 1980, p. 89.*

- [6] Reza Asgari, "Semiconductor backend flip chip processing, inspection requirements and challenges", *Electronics Manufacturing Technology Symposium*, pp. 18-22, June 2002.
- [7] Jon Titus, "Keep Your Eye on the Metal Bumps", *Test and Measurement World*, June 2005
- [8] Sakuma, H., "Interferometry for rough surface", *International Conference on Lasers and Electro-Optics Europe*, pp. 230-235, Sept. 2000.
- [9] Deborah S. Patterson, Peter Elenius, "wafer bumping technologies-a comparative analysis of solder deposition processes and assembly considerations", *Flip Chip Technologies*.
- [10] Pyunghyun Kim an Sehun Rhee, "Three-dimensional inspection of ball grid array using laser vision system", *IEEE Transactions on Components, Packaging and Manufacturing Technology*, Vol.22, pp.151 - 155, April 1999
- [11] Sumimoto, T., Maruyama, T., Azuma, Y., Goto, S., "Development of image analysis for detection of defects of BGA by using X-ray images", *IEEE Proceedings of IMTC '03. on Instrumentation and Measurement Technology Conference*, Vol.2, pp.1131 - 1136, May 2003.
- [12] Sumimoto, T., Maruyamay, T., Azuma, Y. and Goto, S., "Detection of defects at BGA solder joints by using X-ray imaging", *IEEE ICIT '02. Conference on Industrial Technology Vol.1*, pp. 238 - 241, Dec. 2002.



- [13] Kuk Won Ko, Young Jun Roh and Hyung Suck Cho, "A neural network approach to the inspection of ball grid array solder joints on printed circuit boards", *Proceedings of the IEEE-INNS-ENNS International Joint Conference on Neural Networks Vol.5*, pp.233 - 238, July 2000.
- [14] Li, J., McIntyre, M., Lee, K. and Worster, B., "Production use of an integrated automatic defect classification (ADC) system operating in a laser confocal white light imaging defect review station", *Proceedings on Advanced Semiconductor Manufacturing Conference and Workshop, ASMC 96IEEE/SEMI* pp.107 - 111, Nov. 1996.
- [15] S.Sinzinger and J.Jahns, "Implementation of an integrated confocal sensor using planar optics", *IEEE Transactions on computer vision*, 11(1), pp.215-221, 2000.
- [16] Rideout, E., "BGA inspection", *Proceedings on Electronics Manufacturing Technology Symposium, Vol.1*, pp. 388.
- [17] Miller, M.R., Mohammed, I. and Xiang Dai, "Analysis of flip-chip packages using high resolution moire interferometry", *Proceedings on Electronic Components and Technology Conference*, pp.979 - 986, June 1999.
- [18] Maur, F, "X-ray inspection for electronic packaging latest developments", *International Proceedings Conference on Electronic Packaging Technology*, pp. 235 - 239, Oct. 2003.

- [19] Jong-Soo Lee and Yu-Ho Jeong, "CCD camera calibrations and projection error analysis", *Science and Technology KORUS 2000 Proceedings on the 4th Korea-Russia International Symposium, Vol. 2, pp. 50 - 55, July 2000.*
- [20] Reza Asgari, "Semiconductor backend flip chip processing, inspection requirements and challenges", *Electronics Manufacturing Technology Symposium, pp. 18-22, June 2002.*
- [21] K. Kanatani. "Statistical Optimization for Geometric Computation: Theory and Practice". *Elsevier Science, 1996.*
- [22] Nasrabadi, N.M., Liu, Y. and Chiang, J.L., "Stereo vision correspondence using a multichannel graph matching technique", *IEEE Proceedings on International Conference on Robotics and Automation, Vol.3, pp.1804 -1809, April 1988.*
- [23] Kuan, D., "Constraint and consistency in stereo matching", *IEEE International Conference on Acoustics, Speech, and Signal Processing, Vol.11 ,pp.2079 - 2082, Apr. 1986.*
- [24] Lihi Zelnik-Manor, Michal Irani, "Multiple view on homographies", *IEEE transactions of pattern analysis and machine intelligence, Vol. 24, January, 2002.*
- [25] Luong, Q.-T. and Faugeras, O.D., "Determining the fundamental matrix with planes: instability and new algorithms", *IEEE Proceedings on CVPR*

'93., 15-17, pp.489 - 494, June 1993.

[26] Huttenlocher, D.P. and Lorigo, L.M., "Recognizing three-dimensional objects by comparing two-dimensional images", *IEEE Computer Society Conference on Vision and Pattern Recognition, 1996. Proceedings CVPR*, pp.878 - 884, June 1996.

[27] Criminisi, A., Reid, I., Zisserman, A., "Single view metrology", *Computer Vision, 1999. The Proceedings of the Seventh IEEE International Conference on*

[28] Siwook Nam, Hanjoo Kim, Jaihie Kim, Nicolai Petkov, Michel A. Westenberg, "Trajectory Estimation Based on Globally Consistent Homography", *Proceedings on Computer analysis of images and patterns : 10th international conference, CAIP 2003, Groningen, The Netherlands*, pp.214-222.

[29] Etienne Vincent and Robert Laganeire, "Detecting planar Homographies in an image pair", *Proceeding on 2nd International Symposium on Image and Signal Processing and Analysis*, pp. 182-187, Pula, Croatia, June 2001.

[30] K. Kanatani. "Statistical Optimization for Geometric Computation: Theory and Practice". *Elsevier Science*, 1996.

[31] M.P.Kumar, S.Kuthirummal, C.V.Jawahar, and P.J.Narayanan. "Planar homography from fourier domain representation". In *Proc. International Conference on Signal Processing and Communications (SPCOM)*, 2004

- [32] L. Lucchese. "A hybrid frequency-space domain algorithm for estimating projective transformations of color images". *In Proc. International Conference on Image Processing, volume 2, pages 913-916, 2001.*
- [33] Richard Hartley and Andrew Zisserman, "Multiple View Geometry", *Cambridge University Press, second edition, p138-150*
- [34] Alter. O, Brown. PO, Botstein. D., "Singular value decomposition for genome wide expression data processing and modeling", *Proc Natl Acad Sci U S A, 97, 10101-6.*
- [35] Golub, G. H., and Van Loan, C.F. "Matrix Computations", *Johns Hopkins University Press, 2nd ed., 1989.*
- [36] Shabana, Ahmed A., "Computational dynamics", *New York : Wiley, c1994, pp. 68-81, 1994.*
- [37] I. E. Sutherland. Sketchpad, "A man-machine graphical communications system". *Technical Report 296, MIT Lincoln Laboratories, 1963.*
- [38] R. Hartley. "In Defence of the 8-point Algorithm". *IEEE Transactions on pattern Analysis and Machine Intelligence, 19(6):580-593, 1997.*
- [39] M.A. Fischler and R.C. Bolles, "Random sample consensus: A paradigm for model fitting with application to image analysis and automated cartography", *Communications of the ACM, Vol. 24(6), pp. 381-395, 1981.*



- [40] Q.Luong and T.Vieville, "Canonical Representation for the Geometries of Multiple Views", *Computer Vision and Image Understanding*, 64(2):193-229, 1996.
- [41] L. Lucchese, "A Hybrid Frequency-space Domain Algorithm for Estimating Projective Transformations of Color Images", *In Proc. International Conference on Image Processing*, volume 2, pages 913-916, 2001.
- [42] C. Harris and M. Stephens, "A combined corner and edge detector," *in Proc. 4th Alvey Vision Conference, Manchester, 1988*, pp. 147-151.
- [43] Klaus Strobl, Wolfgang Sepp, etc., "Camera Calibration Toolbox for Matlab", [http://www.vision.caltech.edu/bouguetj/calib\\_doc/](http://www.vision.caltech.edu/bouguetj/calib_doc/)
- [44] A. J. Lacey, N. Pinitkarn and N. A. Thacker, "An evaluation of the performance of RANSAC Algorithms for Stereo Camera Calibration", *Electronic Proceedings of The Eleventh British Machine Vision Conference, University of Bristol, 11-14 September 2000*.
- [45] Zhengyou Zhang, "Camera Calibration with One-Dimensional Objects", *IEEE Transactions on Pattern Analysis and Machine Intelligence*, Vol. 26, pp. 892-899, July 2004.
- [46] Jong-Soo Lee and Yu-Ho Jeong, "CCD camera calibrations and projection error analysis", *Science and Technology KORUS 2000 Proceedings on the 4th Korea-Russia International Symposium*, Vol. 2, pp. 50-55, July 2000.



- [47] Zhou Chuan, Tan Dalong, Zhu Feng “A planar homography estimation method for camera calibration”, *Computational Intelligence in Robotics and Automation, 2003. Proceedings. 2003 IEEE International Symposium on*
- [48] Greg Kochanski, “Monte Carlo Simulation”, <http://kochanski.org/gpk/>



CUHK Libraries



004366630